3.3. Third publication

INORGANIC CHEMISTRY FRONTIERS

CHINESE CHEMICAL SOCIETY

ROYAL SOCIETY OF CHEMISTRY

RESEARCH ARTICLE

Cite this: *Inorg. Chem. Front.*, 2021, **8**, 3803

The effects of the chemical composition on the structural, thermodynamic, and mechanical properties of all-inorganic halide perovskites†

Pablo Sánchez-Palencia, [a,b] Gregorio García, *[a,b] Perla Wahnón [a,b] and Pablo Palacios [a,c]

Organic–inorganic hybrid halide perovskites are widely used in optoelectronic devices, such as solar cells and light-emitting devices. Pursuing solutions to overcome the key problem of instability shown by most used $MAPbI_3$ materials, all-inorganic perovskites like $CsPbI_3$ are attracting considerable attention. Unfortunately, $CsPbI_3$ still suffers from significant issues relating to chemical instability and toxicity due to the presence of Pb atoms; therefore, it is necessary to carry out a profound review of the properties of all-inorganic perovskites to overcome these problems. Experimental laboratories cannot afford, in terms of money and time, to synthesize and characterize large numbers of compounds to rigorously assess the outcomes. Therefore, a systematic density functional theory study of the family of all-inorganic perovskites with the general formula $CsPb_{1-b}Sn_b(I_{1-x}Br_x)_3$ has been performed, covering the entire chemical composition range and elucidating the connections between composition and the structural, thermodynamic, and mechanical properties, in addition to any effects on stability. Our results allow us to gain significant insight in the search for new all-inorganic perovskites with tailored structural, thermodynamic, and mechanical properties *via* fine-tuning the chemical composition.

Received 15th March 2021,
Accepted 26th June 2021

DOI: 10.1039/d1qi00347j

rsc.li/frontiers-inorganic

Introduction

Perovskites have turned out to allow great advances in the photovoltaic field in recent years, showing a record power conversion efficiency (PCE) of 25.2% (29.1% when used in a tandem configuration with Si cells) compared with efficiencies lower than 10% barely 7–8 years ago.[1–5] This vertiginous growth has arisen due to much work by research groups devoted to these materials, mainly hybrid organic–inorganic methylammonium lead iodide (MAPI), which has exhibited the most outstanding efficiencies, and, to a lesser extent, formamidinium lead iodide (FAPI). These studies have been specifically focused on all the properties related to solar efficiency, like band gap,[6] absorption,[7,8] and charge-carrier transport[9,10] and recombination processes,[11,12] among others. However, when analyzing this revolutionary family of materials, besides their PCEs, it is compulsory to look also at their stability, one of the biggest weaknesses of these emerging perovskites that has attracted a lot of attention in recent years.[13–15] Generally, perovskites present instability under the influence of moisture, oxygen, UV light, and heat due to various mechanisms like polymorphic transitions, hydration, oxidation, and decomposition,[16–19] achieving lifetimes of no more than 10 000/1000 h during storage/under illumination during testing.[20] To overcome the gap from laboratory development to reaching the commercial market, stability should be considered as a key criterion when selecting a material,[19,21] while trying not to compromise the properties which lead to high efficiencies. Apart from the utilization of different materials for the different layers and interfaces and the development of diverse device engineering,[15,22–25] the main method for solving this problem involves adjusting the chemical compositions of these materials, introducing new ions by means of partial substitution[13,26,27] or total replacement,[28,29] which allows the properties to be finetuned. For that reason, the effects of chemical composition modification on perovskite stability, assessed based on the structural, thermodynamic, and mechanical properties, need to be further studied.

The formula of a standard perovskite structure, ABX_3, is at this point perfectly well known, where A is a univalent cation,

[a]*Instituto de Energía Solar, ETSI Telecomunicación, Universidad Politécnica de Madrid, Ciudad Universitaria, s/n, 28040 Madrid, Spain. E-mail: ggmoreno@etsit.upm.es*
[b]*Departamento de Tecnología Fotónica y Bioingeniería, ETSI Telecomunicación, Universidad Politécnica de Madrid, Ciudad Universitaria, s/n, 28040 Madrid, Spain*
[c]*Departamento de Física aplicada a las Ingenierías Aeronáutica y Naval. ETSI Aeronáutica y del Espacio, Universidad Politécnica de Madrid, Pz. Cardenal Cisneros, 3, 28040 Madrid, Spain*

†Electronic supplementary information (ESI) available. See DOI: 10.1039/d1qi00347j

B a divalent cation, and X a halogen. Despite efforts aimed at increasing the stabilities of MAPI and FAPI hybrid perovskites, those with the best efficiencies that have been studied for a longer time, the latest research is pointing towards the use of inorganic perovskites,[30–32] trying to solve the stability problems caused by the rotation of the complex organic molecule located at the A position.[33–35] Concretely, the all-inorganic $CsPbI_3$ perovskite is gathering special attention because of its adequate bandgap and stability, although it is identically toxic due to the presence of lead. It is well known that lead s- and p-states play a major role in the high efficiencies already achieved, as they comprise the external levels of the VB and CB, respectively, dominating optical transitions between them.[36] Additionally lead-free perovskites seem to exhibit lower stabilities than their lead-containing counterparts.[20] These facts make it difficult to get rid of this toxic element, although this an established goal that has been thoroughly studied.[37–41] Nevertheless, following this line of research, several compounds have been proposed with promising results, especially through the partial substitution of lead with tin.[42,43] To stabilize the $CsPbI_3$ photoactive perovskite black α-phase, avoiding its spontaneous deformation into the light-inactive yellow δ-phase, which occurs under ambient conditions because cesium cations are too small to hold PbI_6 octahedra,[44,45] different approaches have been used; among these, the partial replacement of iodine with bromine has been carried out,[46–50] considering the idea that a smaller halogen atom will reduce the size of the octahedra. Besides, halogen substitutions change the bandgap but not the shape of the external bands as in the case of lead.[51,52]

This paper is focused on the effects of chemical composition modification on the structural, thermodynamic, and mechanical stabilities of all-inorganic cesium perovskites with the general formula $CsPb_{1-b}Sn_b(I_{1-x}Br_x)_3$. The study of the whole chemical composition range would require a large quantity of experimental work, which would be time- and cost-consuming. Thus, an *ab initio* study based on density functional theory (DFT) calculations allows us to feasibly cover a wide range of chemical compositions, knowing in detail how composition changes will affect the different properties of the perovskites. Some of the compounds proposed herein (those with b = 0.4 and 0.3, and x = 0) have been previously studied as good candidates for use in solar cells.[42,43] Firstly, stability has been assessed through a series of structural tolerance parameters, like the Goldschmidt factor,[53] Sun's parameter,[54] and the bonding strength.[55] Also, thermodynamic stabilities have been evaluated by means of formation enthalpies according to standard procedures, taking into account two different pathways.[56,57] Furthermore, several mechanical properties have been calculated based on the elastic constants of the different compounds obtained from *ab initio* calculations, trying to provide data that are harder to obtain experimentally, as measurements are sometimes complex and difficult to reproduce; this has sometimes led to these properties not having been precisely described. Young's, bulk, and shear moduli and Poisson's ratio data are presented to give an overall picture of the mechanical responses of these materials to different stresses; the responses are important for their integration into complex multilayer devices[58,59] or their use for flexible and wearable applications,[60,61] and they can also have a big impact on absorptivity, which relies on the crystallinity and stress state.[28,29] All of these properties define a complete set that can suitably describe the different facets of the intrinsic stabilities of these halide perovskites, which, to our best knowledge, has not been given up to now, providing details about how to control these properties through composition engineering.

Methodology

Theoretical methods

As mentioned above, this paper is focused on analyzing the effects of chemical composition modifications on several structural, thermodynamic, and mechanical parameters, aimed at evaluating the adequacy integrating the studied perovskites into complex electronic devices. Thus, this section describes the different approaches applied herein to obtain these calculated properties.

To explain better the structural properties, a simple sketch of the perovskite structure is depicted in Fig. 1, paying special attention to the bond-generated octahedra (BX_6 and XCs_4B_2, according to the common and previously proposed nomenclature), whose proportions and dimensions will be of particular

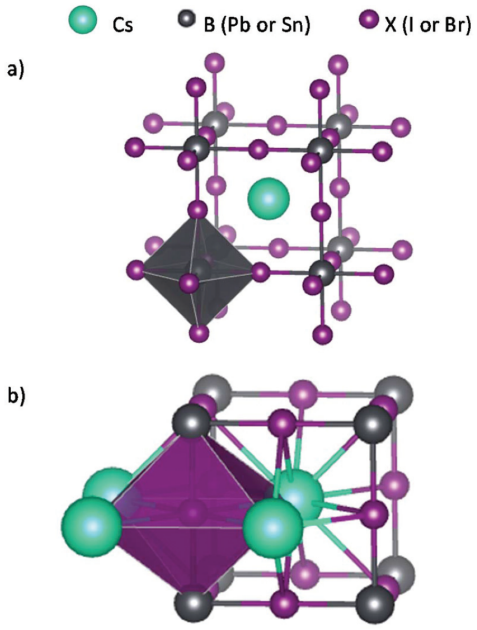

Fig. 1 The structures of perovskite crystals with the different octahedra generated *via* atom bonding highlighted: (a) the BX_6 octahedron and (b) the XCs_4B_2 octahedron.

importance for determining the structural stability of the crystals.

The Goldschmidt tolerance factor (t), used to assess structural stability, is easily determined from ionic radii (r_{Cs}, r_B, and r_X, where the sub-indices indicate the respective positions in the perovskite structure) according to the formula:[62]

$$t = ((r_{Cs} + r_X))/\sqrt{2}(r_B + r_X). \quad (1)$$

When examining B = Pb/Sn and X = I/Br in cases involving partial compositions, the radii of the different ions were weighted according to the concentrations of the different elements occupying equivalent positions. This weighting is needed for many other calculated properties; the way that partial concentrations of elements in equivalent positions are defined from now on is through the use of x and b in the different formulas. Additionally, all the parameters relying on the ionic radii of the different atoms of the compounds have been calculated with the set of radii proposed by Shannon *et al.*[63] Other sets of radii have been used to check the non-reliability of the results from the used set, and all the information on those sets is presented in the ESI.†

Sun *et al.*[54] also proposed an alternative parameter or figure of merit (here denominated as Sun's parameter, ζ) to determine the stability of perovskites based on their structural configuration, improving a correlation factor based on the Goldschmidt parameter previously proposed by Li *et al.*;[64] it additionally considers the octahedral factor μ and the atomic packing factor η according to the following formulas, where a is the lattice parameter of the cell and i is the total number of atoms in it:

$$\zeta = (\mu + t)^{\eta} \quad (2)$$

$$\mu = r_B/r_X \quad (2.1)$$

$$\eta = \sum_i \left(\frac{4}{3}\pi {r_i}^3\right)/a^3. \quad (2.2)$$

The bonding strength (S), which is defined as an isotropic quantity that defines the resistance of a material to bond breaking, has been calculated based on the method first proposed by Šimůnek *et al.*,[65] later modified by Boyko *et al.*,[55] to study ternary compounds with spinel structures; afterwards, it was tailored by us.[66] Šimůnek introduced this concept as an intrinsic parameter in proportion to the hardness of a material, a measurement hard to assess through theoretical calculations due to its complexity and quantity variations according to the experimental methods used for its obtention. This property has been calculated taking into account that in a $CsPb_{1-b}Sn_b(I_{1-x}Br_x)_3$ perovskite, each halide X atom is in an octahedral environment (see Fig. 1b), forming four bonds with Cs atoms in the equatorial plane while two B atoms (Sn or Pb) are located along the longitudinal axis. This way, considering the bond lengths d(X–Cs) and d(X–B) and the average electron density (e_i), the definition of the bonding strength (S) is as follows, with Z_i and R_i being the appropriately weighted electronic valence charge and atomic radius of the corresponding Cs, B, or X atoms:

$$S = \frac{\sqrt{e_X e_{cat}}}{2d_{X-B} + 4d_{X-Cs}} \quad (3)$$

where:

$$e_{cat} = 0.67e_{Cs} + 0.33e_B \quad (3.1)$$

$$e_X = (1 - x)e_I + xe_{Br} \quad (3.2)$$

$$e_B = (1 - b)e_{Pb} + be_{Sn} \quad (3.3)$$

$$e_i = \frac{Z_i}{R_i} (i = Cs, B \text{ or } X) \quad (3.4)$$

$$d_{X-B} = (1 - b)(1 - x)d_{Pb-I} + b(1 - x)d_{Sn-I} + (1 - b) \times d_{Pb-Br} + b \times dS_{n-Br} \quad (3.5)$$

$$d_{X-Cs} = (1 - x)d_{Cs-I} + xd_{Cs-Br}. \quad (3.6)$$

Thermodynamic stability has been assessed through two different pathways. In this approach, standard formation enthalpies (ΔH_f) have been calculated starting from independent constituent elements in their ground states, but values were also obtained considering the standard route from known stable binary compounds, *i.e.*, CsX and BX_2 (named ΔH_s from now on). Despite the different pathways, the standard procedure to obtain formation enthalpies considering the chemical potential μ° has been followed in all cases:[54,57]

$$\Delta H_f = E_{tot}[CsPb_{1-b}Sn_b(I_{1-x}Br_x)_3] - \{\mu^0_{Cs} + (1 - b)\mu^0_{Pb} + b\mu^0_{Sn} + 3[(1 - x)\mu^0_I + x\mu^0_{Br}] \quad (4.1)$$

$$\Delta H_s = E_{tot}[CsPb_{1-b}Sn_b(I_{1-x}Br_x)_3] - (1 - x)\{E_{tot}[CsI] + (1 - b)E_{tot}[PbI_2] + bE_{tot}[SnI_2]\} - x\{E_{tot}[CsBr] + (1 - b)E_{tot}[PbBr_2] + bE_{tot}[SnBr_2]\}. \quad (4.2)$$

In general, a negative enthalpy determines the range of chemical potentials within which the studied compound is thermodynamically stable. The calculated ΔH_f values provide an energy scale that measures the strength of chemical bonding in a compound relative to the strength of bonding in its constituents, while ΔH_s can be related to possible pathways for the synthesis of the material.[31,67,68]

Regarding the mechanical properties, two kinds of VASP calculations have been carried out to obtain all the desired parameters. Firstly, to obtain the bulk modulus, energy/volume variations have been assessed starting from the optimized structures for each compound. In this manner, optimizations at fixed volume for a series of structures covering a range of lattice constants from 0.975 to 1.025 times the optimized value have been done. The resulting energy/volume curve has been fitted to the Birch–Murnaghan equation of state,[69,70] presented below, from which the bulk modulus is deduced. E stands for energy, V for volume, and B for the bulk modulus, while B' is its derivative with respect to pressure; the

sub-index 0 represents the optimized/minimal energy structure:

$$E(V) = E_0 + \frac{9V_0B_0}{16}\left\{\left[\left(\frac{V_0}{V}\right)^{\frac{2}{3}}-1\right]^3 B'_0 + \left[\left(\frac{V_0}{V}\right)^{\frac{2}{3}}-1\right]^2\left[6-4\left(\frac{V_0}{V}\right)^{\frac{2}{3}}\right]\right\}$$

The rest of the parameters have been extracted from stress tensors also calculated with VASP according to the strain-stress methodology implemented in the program.[71,72] In this way, Young's modulus (Y), shear modulus (G), and Poisson's ratio (ν) values are calculated on the basis of elastic constants (c_{ij}), according to Voigt–Reuss–Hill approximations.[73] The bulk modulus (B) is also calculated based on the elastic constant to compare and check that the results are in concordance with those obtained from the fitting to the Birch–Murnaghan equation. The correlations between these parameters and the elastic constants are stated in the following formulas:

$$B = (c_{11} + 2c_{12})/3 \quad (6)$$

$$G = \frac{\{(c_{11} - c_{12} + 3c_{44})/5\} + \{5(c_{11} - c_{12})c_{44}/[4c_{44} + 3(c_{11} - c_{12})]\}}{2} \quad (7)$$

$$Y = \frac{9BG}{3B + G} \quad (8)$$

$$\nu = \frac{3B - 2G}{2(3B + G)} \quad (9)$$

Computational details

The calculations proposed herein have been performed with the Vienna *Ab initio* Simulation Package (VASP). Structural optimizations have been performed using the PBEsol functional,[74] specifically developed for solids and mechanical properties, by means of the conjugate gradient algorithm implemented in the program with forces and total energies converged to 0.01 eV Å^{-1} and 10^{-5} eV, respectively. The Brillouin zone has been sampled using an 8 × 8 × 8 k-point mesh for structural optimization and a 12 × 12 × 12 mesh for static calculations. Structural, thermodynamic, and mechanical properties were calculated using optimized geometries. Additionally, the SCAN functional[75] has been used to obtain accurate final energies for all compounds for thermodynamic analysis. To obtain the elastic constants and mechanical properties, strain-stress methodology has been applied with finite distortions of the lattice, allowing maximum degrees of freedom during subsequent optimization. For this step, the plane-wave cutoffs were increased to 400 eV, way beyond the 30% increment recommended by the system to converge the stress tensor. Considering the more demanding situation, a 4 × 4 × 4 k-point mesh was used at this point, although denser grids were tested with no convergence differences.

$CsPb_{1-b}Sn_b(I_{1-x}Br_x)_3$ perovskites with partial concentrations of group-IV cations and halogens have been studied, with b = 0.0, 0.125, 0.25, 0.5, 0.75, 0.875, and 1.0 and x = 0.0, 0.167, 0.333, 0.5, 0.667, 0.833, and 1.0. For comparison purposes, only the cubic structure, that of the most useful phase for solar applications in the most commonly used $CsPbI_3$ material,[76] has been considered in this work, whether stable at room temperature or not. In the cases of the four ternary compounds, only $CsSnBr_3$ presents a cubic phase that is stable at room temperature,[77–80] although different solutions to this issue have been already proposed.[80–84] All possible chemical configurations for each one of the studied complexes have been generated starting from the 2 × 2 × 2 supercell of $CsPbI_3$ using the combinatorial methodology implemented in the SOD (Site Occupancy Disorder) program,[85] focusing our interest on the structures of each composition with the highest space group symmetry, which are also those with the lowest energy.

Results

Contour maps have been chosen to present the variations in the values of the studied parameters with composition; in this way it is possible to distinguish between the different effects of halogen and cation substitution. For every contour map, a table with all the results from the studied compounds relating to the corresponding property is presented in the ESI.†

Structural parameters

The principal lattice parameter values for the fully optimized structures are presented in Fig. 2a. Considering distortion during the optimization of some of the structures from the initial cubic cell to a tetragonal lattice, the a/c ratio values are also display in Fig. 2b, and the cell volumes are shown in Fig. 2c. It must be noted that all the values relate to the 40-atom cells used to deal with the wide range of concentrations. The obtained values for the four ternary compounds agree with an average deviation of 0.725%, and in all cases the values deviate by less than 1.2% from experimental results,[78,86,87] improving the calculated parameters from The Materials Project database,[88] which show an average deviation of 1.782%; this supports the results presented here and the use of the PBEsol functional (the Materials Project results are calculated with the standard PBE functional).

It can be seen that the cation concentration barely affects the parameters, especially the a/c parameter, which remains almost unaffected by this factor. For the lattice parameter a, the tendency when lead is totally replaced by tin is to show a small decrease, with total variations lower than 2% from one extreme to the other, while for the volume the tendency is also to decrease, by less than 5.5%.

On the other hand, changing the halogen concentration results in a variation in volume of around 20% from one extreme (only iodine) to the other (only bromine), with a very uniform decrease; the $CsSnBr_3$ perovskite has the smallest value

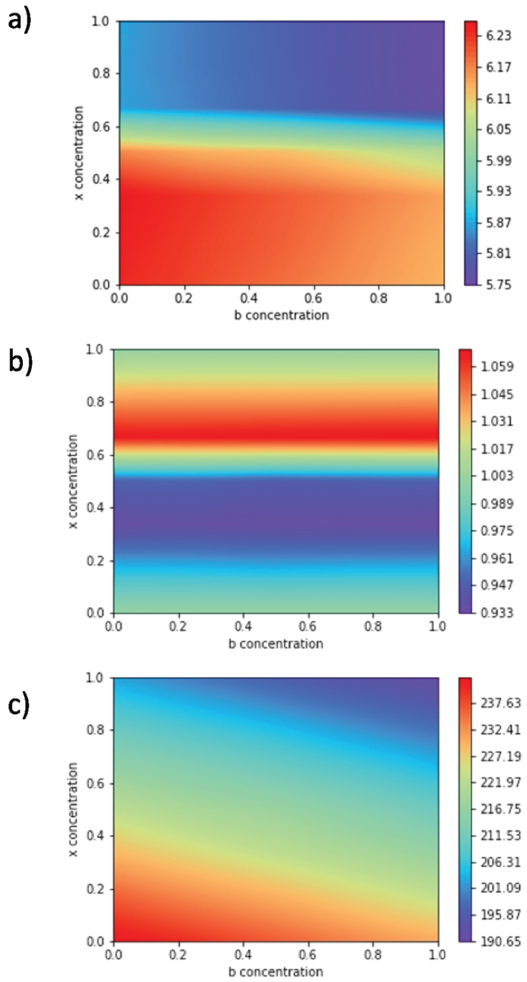

Fig. 2 (a) Lattice constant a [Å], (b) shape ratio a/c [dimensionless], and (c) volume [Å^3] data for the unit cells of $CsPb_{1-b}Sn_b(I_{1-x}Br_x)_3$ perovskites. For more details relating to calculated numerical values as a function of chemical composition, see the ESI.†

and $CsPbI_3$ has the biggest value, as expected according to the sizes of the atoms. Nevertheless, the uniform decrease seen in the volume values is not as uniform when it comes to shape. As was previously mentioned, a perfect cubic structure is not retained except in the cases of pure iodine and bromine perovskites, and the partially substituted ones are slightly distorted into a tetragonal shape. For structures with high concentrations of iodine the crystals adopt a progressively shortened (a/c lower than 1) tetragonal form, with the minimum a/c value equal to 0.935 when x = 0.33, while at high concentrations of bromine the crystals become stretched tetragonal cells (a maximum a/c value of 1.065 at x = 0.66). Thus, a/c value decreases upon x increasement for lower (x = 0.00–0.33) and higher (x = 0.66–1.00) bromine concentrations. On the contrary, for intermediate x concentrations (x = 0.33–0.66), a/c value increases with x. The main lattice constant also shows a non-uniform decrease of nearly 6% as x changes from 0 to 1. The concentration ranges where the a/c parameter decreases also relate to slight changes in the lattice constant (x = 0–0.33 and x = 0.66–1), while for the range where the a/c ratio increases (x = 0.33–0.66), a rapid decrease occurs. Thus, it could be said that these variations balance out the non-uniform shape change trend, giving room for the resulting uniform volume decrease.

Besides basic distortions of the volume and shape of the structure, the relative atom positions, *i.e.*, the distances between bonded atoms, are important in terms of the structural stability of the perovskite. The Goldschmidt tolerance factor has been extensively used to easily assess the stabilities of perovskites in similar terms, ensuring that the sizes of the different atoms are balanced so as not to distort the structure in excess, which could lead to bond breaking and different structures. The bonding strength also determines how easily the structure could collapse based on the distances between different atoms.

The Goldschmidt factor graph is presented in Fig. 3a. Values between 0.8 and 1 are supposed to be associated with perovskites that have a good chance of be formed, with all analyzed structures lying within these limits.[62] This preliminary check is useful for gaining a perspective of the magnitude of the shape distortions observed above, showing that these are not large enough to cause structural instability. In this case the effect of b modification is greater than that of x modification; this is because the main use of this parameter is to evaluate the equilibrium in size between both types of cations, and therefore the radius of the halogen is less important. This

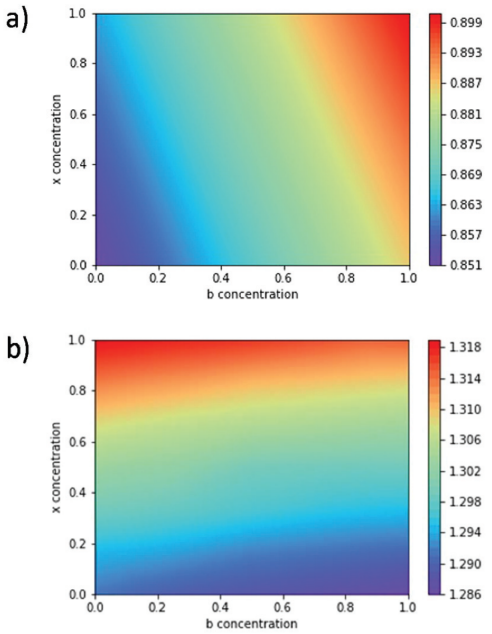

Fig. 3 (a) The Goldschmidt tolerance parameter [dimensionless] and improved (b) Sun's parameter [dimensionless] values for $CsPb_{1-b}Sn_b(I_{1-x}Br_x)_3$ perovskites. For more details on the calculated numerical values as a function of the chemical composition, see the ESI.†

fact is shown by the formula, where halogen atom radius is present in both terms, unlike the B atom radius. The highest value, which means the most stable compound in theory, belongs to $CsSnBr_3$ (0.90), while the minimum value corresponds to $CsPbI_3$ (0.85), although this is still far from the frontier of stability marked by a value of 0.8. From this point of $CsPbI_3$, a uniform increase with x is observed, while the same trend occurs across the b range. As they depend exclusively on the radii of the different atoms and, consequently, on the chosen set of radius values, the Goldschmidt factor values for the four ternary compounds agree well with previous results taken from the literature when Shannon radii are also used,[54,89] although precise correlation is not observed because of the different coordination environments considered. This decision is discussed in more detail in the ESI.†

The Sun's parameter values, presented in Fig. 3b, should have better correlation with the thermodynamic stability of the perovskites, and this will be assessed in the following discussion. In this case it is observed that the most stable zone for Sun's parameter lies in the region of $CsPbBr_3$ because of the octahedral factor influence. In this case, the influence of x on the parameter is greater than that of b, and the maximum value is obtained from the perovskite $CsPbBr_3$.

Again, an increase as the x concentration changes from 0 to 1 occurs, but in this case the property value decreases as the b value increases, mainly relying upon the octahedral factor, which exhibits the same trend. Despite the opposing trends, both variations are essentially continuous within the studied range.

The bonding strength is defined as an isotropic quantity that defines the resistance of a material to bond breaking. The values of this parameter for the studied compounds are presented in Fig. 4.

As chemical intuition dictates, the presence of smaller atoms in the perovskite leads to greater bonding strength, taking into account that the valence charges of atoms in equivalent positions are the same. It is interesting to note that while the Goldschmidt factor is mostly influenced by b, bonding strength is more affected by x, which seems reasonable considering that the halogen atoms have greater presence and are part of every single bond. To the contrary, as previously mentioned, the Goldschmidt factor indicates how balanced the sizes of both cations are, being less affected by the halogens involved in the bonds. In this case the variation along the x concentration range involves an increase of around 13.1%, while the rise along the b concentration axis is approximately 4.7%; both trends are continuous. Small deviations from the linear trends, falling in all cases within a negligible ±0.5% range, are explained based on the uncertainty of the calculations, corresponding to insignificant displacements of the cell or the positions and, consequently, distances between atoms, or, directly, to the averages of these distances for all atoms in the cell, resulting in differences of a few hundredths of an Angstrom.

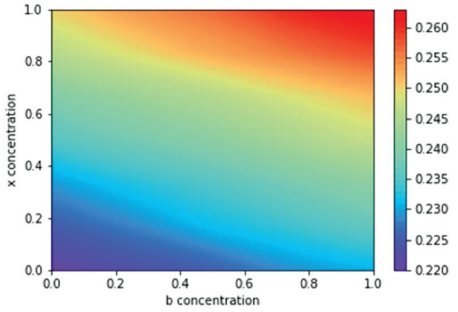

Fig. 4 Bonding strength [dimensionless] values for $CsPb_{1-b}Sn_b(I_{1-x}Br_x)_3$ perovskites. For more details on the calculated numerical values as a function of the chemical composition, see the ESI.†

Thermodynamic parameters

The most common way to assess the stability of a certain compound is through studying its formation enthalpy. To do that rigorously, it is necessary to evaluate the possible synthesis and decomposition pathways of that compound, considering both the fundamental elements and competitor binary or ternary phases. These enthalpies can be calculated using formulas (4.1) and (4.2), which detail formation enthalpy from fundamental elements (Fig. 5a) and formation or synthesis enthalpy from binary phases (Fig. 5b), respectively. As was previously mentioned, the calculations used to obtain all these energies were carried out with the SCAN hybrid functional.

Herein, the studied perovskites fall way below the stability limits defined by their constituent elements, which means that their formation is plausible from a thermodynamic point

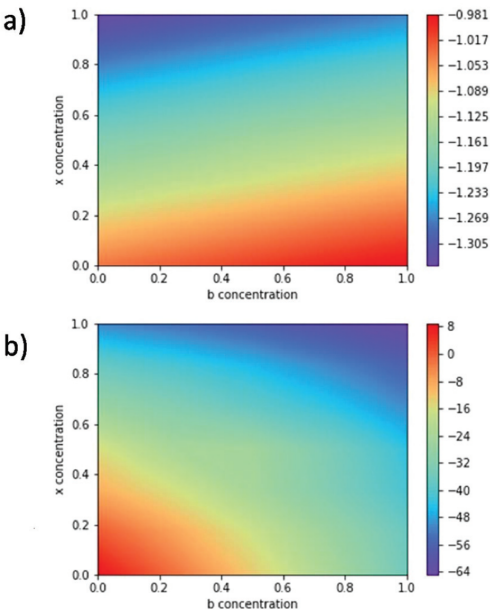

Fig. 5 Formation enthalpies considering (a) constituent elements [eV per atom] and (b) binary compounds [meV per atom] for $CsPb_{1-b}Sn_b(I_{1-x}Br_x)_3$ perovskites. For more details on the calculated numerical values as a function of the chemical composition, see the ESI.†

of view. The very low values presented, in the range of 1–1.2 eV per atom, imply that the perovskite structure is strongly favored energetically. For the case of the enthalpies relating to the binary precursors route, negative values also indicate good stability, discarding in principle metastability with respect to competitor binary compounds, except for perovskites with a clear majority of Pb and I, which could present metastability with very small positive values of less than 10 meV per atom.

The formation enthalpy ΔH_f evolves with a uniform decrease of 29% as x is increased from one extreme to the other, while the corresponding variation is observed when b is modified from 0 to 1, with a uniform rise of 5%. In contrast to that variation, the enthalpy from binary compounds ΔH_s presents a not entirely uniform decrease as Br is introduced. That decrease is progressive, being more pronounced as x increases. At the same time, the effect of the introduction of Br is less significant as the b concentration increases, with a decrease of −60 meV per atom for pure Pb perovskites and −29 meV per atom for pure Sn perovskites. In a similar way, there is a decrease in ΔH_s as b increases, although in this case it is uniform, with a more marked variation for pure I perovskites (−45 meV per atom) than for pure Br ones (−14 meV per atom), and with a progressive change for intermediate examples. In addition, there is a clear trend where highly mixed halogen compounds (x = 0.5) exhibit a small deviation to higher values of formation energy in the binary case, indicating that some instability originates from lattice distortions; on the contrary, this is not seen in the formation energy data based on constituent elements.

In summary, the higher bonding energies of lead binary compounds when compared to tin compounds, as crystalline lead is less energetic than tin, explain why $CsSnBr_3$ and most closed perovskites are those with the lowest ΔH_s values, *i.e.*, the most stable from a binary compound perspective, while the area surrounding $CsPbBr_3$ contains the perovskites with the lowest formation enthalpies from a constituent element perspective. The total energy values obtained directly from the calculations performed herein and the formation enthalpies based on constituent elements calculated using eqn (4.2) agree with reference values obtained from the Materials Project database,[88] within error margins of 1 and 4%, respectively, despite different functionals being employed for the calculations, verifying the results presented here.

At this point is useful to point out the correlation between these two formation-enthalpy types and Sun's parameter and the bonding strength, respectively, as presented in Fig. 6. To measure how good these correlations are, two important statistical indexes are presented: the coefficient of determination (R^2) and the mean absolute error (MAE). Both values are also presented in Fig. 6.

For the prediction of the formation enthalpy from fundamental elements using Sun's parameter, the descriptor works extremely well, with R^2 equal to 0.993 and a MAE of 6.8 meV per atom. Meanwhile, for the formation enthalpy from binary compounds, the R^2 value of 0.896 is not that good, although it is high enough to perform perfectly well, but the MAE is even lower than the previous example, with a value of 4.5 meV per atom, which falls within the 5% threshold. As stated by Sun *et al.*,[54] the correction to the Goldschmidt factor made *via* the inclusion of octahedral and atomic packing factors substantially improves the correlation with the formation enthalpy (given that no correlation could be appreciated using the Goldschmidt tolerance factor in this case), as it takes into account the main structural requirements of the perovskite in terms of the relative sizes of the constituent atoms that are not disrupted by excessively high interatomic forces. At the same time, it makes a lot of sense that the bonding strength, as a measure of the difficulty of breaking bonds, presents a well-adjusted relationship with the formation enthalpy from binary precursors, thinking of that as the usual decomposition pathway of a perovskite and considering that the breaking of bonds is what usually triggers the decomposition process. All these factors confirm the correct performance of these two structural parameters as predictors of perovskite thermodynamics, both being much easier to obtain than a complete thermodynamic study when numerous compounds are going to be studied or multiple calculations are required.

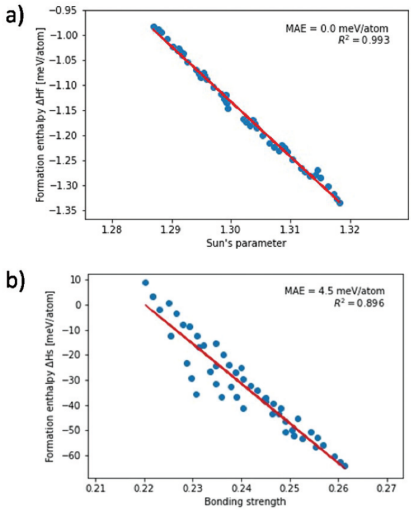

Fig. 6 Correlation between structural and thermodynamic parameters. (a) Formation enthalpy [eV per atom] *vs.* Sun's parameter [dimensionless] and (b) formation enthalpy from binary compounds [meV per atom] *vs.* the bonding strength [dimensionless] for all studied $CsPb_{1-b}Sn_b(I_{1-x}Br_x)_3$ perovskites.

Mechanical parameters

Having good mechanical properties is always an excellent indicator of the suitability of a material for use in complex devices, where it is subject to different stresses. As previously stated, good mechanical stability is also needed by absorber materials to retain absorptivity values and not to present large losses of efficiency over time. Especially important in these cases is the bulk modulus, which determines the stiffness of the material toward compression forces, such as the ones seen in typical multilayer devices, like solar cells, during the manufacturing

process and operation. The values of this property for the different studied compounds are presented in Fig. 7, calculated using the Birch–Murnaghan equation. The bulk modulus has also been calculated from the elastic constants of the materials (see the ESI†); both methods give similar results in terms of trends, although the values are slightly lower when calculated using the Birch–Murnaghan equation, with an average ratio of 1.12 between the values calculated with each method and a highest ratio of 1.22.

From Fig. 7 is possible to see that the maximum value corresponds to the $CsSnBr_3$ perovskite, as for the other parameters relating to stability, with a value of 22.38 GPa. The minimum value corresponds to $CsPbI_3$ (17.46 GPa), which means that the bulk modulus grows with increases in x and b, with almost uniform growth rates of 23.5% and 4.0%, respectively. Once again, all the structures with a halogen composition (x) of 0.5, *i.e.*, the same amounts of I and Br, present an anomalous decrease in the bulk modulus, which can probably be explained, as in the previous case, by the greater distortion of the crystal structure, which gives rise to a worse response to stress, as all those anomalies are related to some type of additional instability.

Some other mechanical properties, like the shear modulus, which determines the shear stiffness, and the Young's modulus, which measures the tensile stiffness, have been also been calculated by means of strain-stress methodology,[71,72] and the results are presented in Fig. 8.

Both parameters, the shear and Young's moduli, present similar trends when the chemical composition is changed. In general, upon x modification, uniform increases at average rates of 25.9% and 26.5%, respectively, from the pure-I to pure-Br extremes are shown, whereas b modification leads to much lesser changes. From $b = 0$ to $b = 0.17$, a rapid decrease is observed, but from that point up to $b = 1$, the trend changes and the value starts to rise quite uniformly until it reaches a value within a range of ±4% of the initial value for the pure-Pb perovskite with the same x concentration. The minimum values at $b = 0.17$ (except for $x = 0.5$, where it lies at $b = 0.33$) for the Shear/Young's moduli show relative values of around 96%/95% of the initial values at $b = 0$, with a minimum value of 94.6%/92.9% when $x = 1/x = 0$.

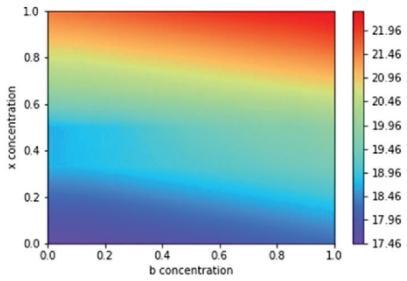

Fig. 7 Bulk modulus [GPa] values for all $CsPb_{1-b}Sn_b(I_{1-x}Br_x)_3$ perovskites studied. For more details about the calculated numerical values as a function of the chemical composition, see the ESI.†

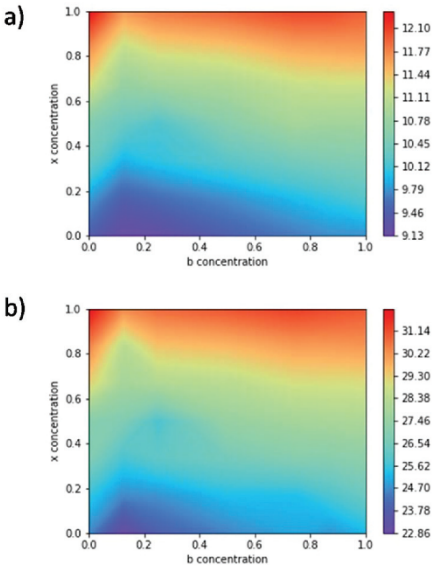

Fig. 8 (a) Shear [GPa] and (b) Young's modulus [GPa] values for all $CsPb_{1-b}Sn_b(I_{1-x}Br_x)_3$ perovskites studied. For more details about the calculated numerical values as a function of the chemical composition, see the ESI.†

Poisson's ratio, which measures the deformation in a direction perpendicular to the load, has been also calculated. Poisson's ratio yields an almost constant value of around 0.29 for the entire composition range. For the sake of simplicity, a contour plot presenting Poisson's ratio values has been omitted (see the ESI† for more details).

All of the studied compounds meet the elastic stability criteria, defined according to the elastic constants for the most general case of symmetry, where: $c_{11} > 0$, $c_{22} > 0$, $c_{33} > 0$, $c_{44} > 0$, $c_{55} > 0$, $c_{66} > 0$, $c_{11} + c_{22} - 2c_{12} > 0$, $c_{11} + c_{33} - 2c_{13} > 0$, $c_{22} + c_{33} - 2c_{23} > 0$; and $c_{11} + c_{22} + c_{33} + 2c_{12} + 2c_{13} + 2c_{23} > 0$.[29] Pugh's criterion[90] is also met, locating all the compounds out of the brittle area and classifying them as ductile materials.[91]

To measure the accuracy of these properties values is delicate, because great differences far beyond the standard 5% error limit in comparison with previously reported values can be seen in the extensive literature in this area,[38,92] especially those relying on different simulation programs. Moreover, the high instability of these compounds when they are manipulated makes it almost impossible to measure these properties experimentally. In spite of that, looking at other works, trends with regard to the four ternary compounds analyzed herein are correctly reproduced in this work, and the property values fall within a similar range to previously reported examples.[38,92–98]

Conclusions

A whole set of properties for the $CsPb_{1-b}Sn_b(I_{1-x}Br_x)_3$ family of all-inorganic perovskites is presented in this work. The main structural, thermodynamic, and mechanical parameters

related to some extent to the intrinsic stabilities of these materials are properly described. It is expected that this set can help researchers, guiding their experimental efforts towards a specific compound depending on the precise properties desired. In this sense, the main parameters evaluated here show that $CsSnBr_3$ is the most intrinsically stable perovskite within the studied range, as indicated by the Goldschmidt factor, the bonding strength, the formation enthalpy based on binary components, and the bulk modulus. Nevertheless, all the compounds studied herein fall within the intrinsic stability region delineated by those parameters.

Regarding all the described properties and the changes that they exhibit upon chemical composition modification, some trends and anomalies are remarkable enough to be compiled and highlighted below:

- Despite the cell volume presenting constant variations when the chemical composition is modified based on the atom radii, the lattice constant of the cell and, consequently, its shape do not present that same trend, losing the cubic structure when mixed halogens are introduced.
- Although most of the properties present a linear dependence on the chemical composition, the formation enthalpy based on binary precursors presents a rather exponential dependence because of the highest stability being shown by lead binary compounds.
- Paying attention to the percentage changes of the different properties, x seems to have considerably more influence than b, which seems logical when looking at the stoichiometry.
- For many properties, especially for those most directly related to stability, like Sun's parameter, the formation enthalpy ΔH_s, and different mechanical parameters, an anomalous deviation from linear trends in the direction of additional instability is observed for most compounds when $x = 0.5$, indicating that the loss of cell symmetry could produce significant but not conclusive instability in these compounds.

Correlation between some structural and thermodynamic parameters is also presented. In one case, the linear dependence of Sun's parameter on the formation enthalpy of the set of compounds studied herein has been confirmed. In another case, new correlation, which has not been previously proposed, between the bonding strengths of the compounds and their formation enthalpies based on binary phases has been verified, with very high rates of correspondence.

Thus, this work offers fundamental insight in the search for new all-inorganic perovskites with tailored structural, thermodynamic, and mechanical properties and reduced toxicity, with a focus on suitable chemical compositions.

Conflicts of interest

The authors declare that they have no known competing financial interests or personal relationships that could have appeared to influence the work reported in this paper.

Acknowledgements

This work was supported by the Ministerio de Ciencia e Innovación through the project BESTMAT-QC (PID2019-107137RB-C22). The authors gratefully acknowledge the Universidad Politécnica de Madrid (www.upm.es) for providing computing resources on Magerit Supercomputer. The statements made herein are solely the responsibility of the authors.

References

1 J. J. Yoo, S. Wieghold, M. C. Sponseller, M. R. Chua, S. N. Bertram, N. T. P. Hartono, J. S. Tresback, E. C. Hansen, J. P. Correa-Baena, V. Bulović, T. Buonassisi, S. S. Shin and M. G. Bawendi, An interface stabilized perovskite solar cell with high stabilized efficiency and low voltage loss, *Energy Environ. Sci.*, 2019, **12**, 2192.

2 P. Tockhorn, P. Wagner, L. Kegelmann, J. C. Stang, M. Mews, S. Albrecht and L. Korte, Three-Terminal Perovskite/Silicon Tandem Solar Cells with Top and Interdigitated Rear Contacts, *ACS Appl. Energy Mater.*, 2020, **3**, 1381.

3 J. H. Heo, S. H. Im, J. H. Noh, T. N. Mandal, C. S. Lim, J. A. Chang, Y. H. Lee, H. J. Kim, A. Sarkar, M. K. Nazeeruddin, M. Grätzel and S. Il Seok, Efficient inorganic-organic hybrid heterojunction solar cells containing perovskite compound and polymeric hole conductors, *Nat. Photonics*, 2013, **7**, 486.

4 NREL, Best Research-Cell Efficiency Chart, https://www.nrel.gov/pv/assets/pdfs/best-research-cell-efficiencies.20200311.pdf, (accessed 21 March 2020).

5 J. P. Correa-Baena, A. Abate, M. Saliba, W. Tress, T. J. Jacobsson, M. Grätzel and A. Hagfeldt, The rapid evolution of highly efficient perovskite solar cells, *Energy Environ. Sci.*, 2017, **10**, 710.

6 T. Wang, B. Daiber, J. M. Frost, S. A. Mann, E. C. Garnett, A. Walsh and B. Ehrler, Indirect to direct bandgap transition in methylammonium lead halide perovskite, *Energy Environ. Sci.*, 2017, **10**, 509.

7 A. Jiménez-Solano, S. Carretero-Palacios and H. Míguez, Absorption enhancement in methylammonium lead iodide perovskite solar cells with embedded arrays of dielectric particles, *Opt. Express*, 2018, **26**, A865.

8 M. D. Nelson and M. Di Vece, Using a neural network to improve the optical absorption in halide perovskite layers containing core-shells silver nanoparticles, *Nanomaterials*, 2019, **9**, 437.

9 A. Filippetti, A. Mattoni, C. Caddeo, M. I. Saba and P. Delugas, Low electron-polar optical phonon scattering as a fundamental aspect of carrier mobility in methylammonium lead halide CH3NH3PbI3 perovskites, *Phys. Chem. Chem. Phys.*, 2016, **18**, 15352.

10 G. Xing, N. Mathews, S. Sun, S. S. Lim, Y. M. Lam, M. Graẗzel, S. Mhaisalkar and T. C. Sum, Long-range

balanced electron-and hole-transport lengths in organic-inorganic CH3NH3PbI3, *Science*, 2013, **342**, 344.
11 Y. Wang, W.-H. Fang, R. Long and O. V. Prezhdo, Symmetry Breaking at MAPbI3 Perovskite Grain Boundaries Suppresses Charge Recombination: Time-Domain ab Initio Analysis, *J. Phys. Chem. Lett.*, 2019, **10**, 1617.
12 M. B. Johnston and L. M. Herz, Hybrid Perovskites for Photovoltaics: Charge-Carrier Recombination, Diffusion, and Radiative Efficiencies, *Acc. Chem. Res.*, 2016, **49**, 146.
13 T. D. Siegler, D. W. Houck, S. H. Cho, D. J. Milliron and B. A. Korgel, Bismuth Enhances the Stability of CH 3 NH 3 PbI 3 (MAPI) Perovskite under High Humidity, *J. Phys. Chem. C*, 2019, **123**, 963.
14 G. Niu, W. Li, J. Li, X. Liang and L. Wang, Enhancement of thermal stability for perovskite solar cells through cesium doping, *RSC Adv.*, 2017, **7**, 17473.
15 T. T. Ava, A. Al Mamun, S. Marsillac and G. Namkoong, A review: Thermal stability of methylammonium lead halide based perovskite solar cells, *Appl. Sci.*, 2019, **9**, 188.
16 M. G. Ju, M. Chen, Y. Zhou, J. Dai, L. Ma, N. P. Padture and X. C. Zeng, Toward Eco-friendly and Stable Perovskite Materials for Photovoltaics, *Joule*, 2018, **2**, 1231.
17 Y. Zhou and Y. Zhao, Chemical stability and instability of inorganic halide perovskites, *Energy Environ. Sci.*, 2019, **12**, 1495.
18 Q. Wali, F. J. Iftikhar, M. E. Khan, A. Ullah, Y. Iqbal and R. Jose, Advances in stability of perovskite solar cells, *Org. Electron.*, 2020, **78**, 105590.
19 Q. Fu, X. Tang, B. Huang, T. Hu, L. Tan, L. Chen and Y. Chen, Recent Progress on the Long-Term Stability of Perovskite Solar Cells, *Adv. Sci.*, 2018, **5**, 1700387.
20 A. Urbina, The balance between efficiency, stability and environmental impacts in perovskite solar cells: a review, *J. Phys. Energy*, 2020, **2**, 022001.
21 M. J. Hong, S. R. Svadlenak, K. A. Goulas and J. G. Labram, Thermal stability of mobility in methylammonium lead iodide, *J. Phys. Mater.*, 2019, **3**, 014003.
22 N. Rolston, K. A. Bush, A. D. Printz, A. Gold-Parker, Y. Ding, M. F. Toney, M. D. McGehee and R. H. Dauskardt, Engineering Stress in Perovskite Solar Cells to Improve Stability, *Adv. Energy Mater.*, 2018, **8**, 1.
23 J. Kim, A. Ho-Baillie and S. Huang, Review of Novel Passivation Techniques for Efficient and Stable Perovskite Solar Cells, *Sol. RRL*, 2019, **3**, 1.
24 Y. Wu, W. Chen, G. Chen, L. Liu, Z. He and R. Liu, The impact of hybrid compositional film/structure on organic–inorganic perovskite solar cells, *Nanomaterials*, 2018, **8**, 1.
25 H. Dong, S. Pang, Y. Zhang, D. Chen, W. Zhu, H. Xi, J. Chang, J. Zhang, C. Zhang and Y. Hao, Improving electron extraction ability and device stability of perovskite solar cells using a compatible PCBM/AZO electron transporting bilayer, *Nanomaterials*, 2018, **8**, 720.
26 P. N. Rudd and J. Huang, Metal Ions in Halide Perovskite Materials and Devices, *Trends Chem.*, 2019, **1**, 394.
27 J. H. Noh, S. H. Im, J. H. Heo, T. N. Mandal and S. Il Seok, *Nano Lett.*, 2013, **13**, 1764–1769.
28 S. Sun, Y. Fang, G. Kieslich, T. J. White and A. K. Cheetham, Mechanical properties of organic-inorganic halide perovskites, CH3NH3PbX3 (X=I, Br and Cl), by nanoindentation, *J. Mater. Chem. A*, 2015, **3**, 18450.
29 J. Feng, Mechanical properties of hybrid organic-inorganic CH3NH 3BX3 (B=Sn, Pb; X=Br, I) perovskites for solar cell absorbers, *APL Mater.*, 2014, **2**, 081801.
30 T. Ma, S. Wang, Y. Zhang, K. Zhang and L. Yi, The development of all-inorganic CsPbX3 perovskite solar cells, *J. Mater. Sci.*, 2020, **55**, 464.
31 J. Duan, H. Xu, W. E. I. Sha, Y. Zhao, Y. Wang, X. Yang and Q. Tang, Inorganic perovskite solar cells: An emerging member of the photovoltaic community, *J. Mater. Chem. A*, 2019, **7**, 21036.
32 Q. Tai, K. C. Tang and F. Yan, Recent progress of inorganic perovskite solar cells, *Energy Environ. Sci.*, 2019, **12**, 2375.
33 A. Mattoni, A. Filippetti, M. I. Saba and P. Delugas, Methylammonium Rotational Dynamics in Lead Halide Perovskite by Classical Molecular Dynamics: The Role of Temperature, *J. Phys. Chem. C*, 2015, **119**, 17421.
34 M. A. Carignano, A. Kachmar and J. Hutter, Thermal effects on CH3NH3PbI3 perovskite from Ab initio molecular dynamics simulations, *J. Phys. Chem. C*, 2015, **119**, 8991.
35 M. Mladenović and N. Vukmirović, Effects of thermal disorder on the electronic structure of halide perovskites: Insights from MD simulations, *Phys. Chem. Chem. Phys.*, 2018, **20**, 25693.
36 A. Filippetti and A. Mattoni, Hybrid perovskites for photovoltaics: Insights from first principles, *Phys. Rev. B: Condens. Matter Mater. Phys.*, 2014, **89**, 1.
37 W. Ke and M. G. Kanatzidis, Prospects for low-toxicity lead-free perovskite solar cells, *Nat. Commun.*, 2019, **10**, 1.
38 M. Roknuzzaman, K. K. Ostrikov, H. Wang, A. Du and T. Tesfamichael, Towards lead-free perovskite photovoltaics and optoelectronics by ab-initio simulations, *Sci. Rep.*, 2017, **7**, 1.
39 F. Giustino and H. J. Snaith, Toward Lead-Free Perovskite Solar Cells, *ACS Energy Lett.*, 2016, **1**, 1233.
40 C. Gai, J. Wang, Y. Wang and J. Li, The low-dimensional three-dimensional tin halide perovskite: Film characterization and device performance, *Energies*, 2020, **13**, 2.
41 L. Serrano-Lujan, N. Espinosa, T. T. Larsen-Olsen, J. Abad, A. Urbina and F. C. Krebs, Tin- and lead-based perovskite solar cells under scrutiny: An environmental perspective, *Adv. Energy Mater.*, 2015, **5**, 1.
42 M. Hu, M. Chen, P. Guo, H. Zhou, J. Deng, Y. Yao, Y. Jiang, J. Gong, Z. Dai, Y. Zhou, F. Qian, X. Chong, J. Feng, R. D. Schaller, K. Zhu, N. P. Padture and Y. Zhou, Sub-1.4 eV bandgap inorganic perovskite solar cells with long-term stability, *Nat. Commun.*, 2020, **11**, 1.
43 Z. Yang, X. Zhang, W. Yang, G. E. Eperon and D. S. Ginger, Tin–Lead Alloying for Efficient and Stable All-Inorganic Perovskite Solar Cells, *Chem. Mater.*, 2020, **32**, 2782.
44 L. Chen, L. Wan, X. Li, W. Zhang, S. Fu, Y. Wang, S. Li, H. Q. Wang, W. Song and J. Fang, Inverted All-Inorganic CsPbI2Br Perovskite Solar Cells with Promoted Efficiency and Stability by Nickel Incorporation, *Chem. Mater.*, 2019, 2.

45 Z. Zeng, J. Zhang, X. Gan, H. Sun, M. Shang, D. Hou, C. Lu, R. Chen, Y. Zhu and L. Han, In Situ Grain Boundary Functionalization for Stable and Efficient Inorganic CsPbI2Br Perovskite Solar Cells, *Adv. Energy Mater.*, 2018, **8**, 1.

46 R. J. Sutton, G. E. Eperon, L. Miranda, E. S. Parrott, B. A. Kamino, J. B. Patel, M. T. Hörantner, M. B. Johnston, A. A. Haghighirad, D. T. Moore and H. J. Snaith, Bandgap-Tunable Cesium Lead Halide Perovskites with High Thermal Stability for Efficient Solar Cells, *Adv. Energy Mater.*, 2016, **6**, 1.

47 S. Mariotti, O. S. Hutter, L. J. Phillips, P. J. Yates, B. Kundu and K. Durose, Stability and Performance of CsPbI2Br Thin Films and Solar Cell Devices, *ACS Appl. Mater. Interfaces*, 2018, **10**, 3750.

48 Y. Wang, T. Zhang, F. Xu, Y. Li and Y. Zhao, A Facile Low Temperature Fabrication of High Performance CsPbI2Br All-Inorganic Perovskite Solar Cells, *Sol. RRL*, 2018, **2**, 1.

49 K. Wang, Z. Jin, L. Liang, H. Bian, D. Bai, H. Wang, J. Zhang, Q. Wang and L. Shengzhong, All-inorganic cesium lead iodide perovskite solar cells with stabilized efficiency beyond 15%, *Nat. Commun.*, 2018, **9**, 1.

50 G. Yin, H. Zhao, H. Jiang, S. Yuan, T. Niu, K. Zhao, Z. Liu and S. (Frank) Liu, Precursor Engineering for All-Inorganic CsPbI2Br Perovskite Solar Cells with 14.78% Efficiency, *Adv. Funct. Mater.*, 2018, **28**, 1.

51 E. Mosconi, A. Amat, M. K. Nazeeruddin, M. Grätzel and F. De Angelis, First-principles modeling of mixed halide organometal perovskites for photovoltaic applications, *J. Phys. Chem. C*, 2013, **117**, 13902.

52 W. J. Yin, Y. Yan and S. H. Wei, Anomalous alloy properties in mixed halide perovskites, *J. Phys. Chem. Lett.*, 2014, **5**, 3625.

53 V. M. Goldschmidt, Die Gesetze der Krystallochemie, *Naturwissenschaften*, 1926, **14**, 477.

54 Q. Sun and W. J. Yin, Thermodynamic Stability Trend of Cubic Perovskites, *J. Am. Chem. Soc.*, 2017, **139**, 14905.

55 T. D. Boyko and A. Moewes, The hardness of group 14 spinel nitrides revisited, *J. Ceram. Soc. Jpn.*, 2016, **124**, 1063.

56 A. M. Deml, R. O'Hayre, C. Wolverton and V. Stevanović, Predicting density functional theory total energies and enthalpies of formation of metal-nonmetal compounds by linear regression, *Phys. Rev. B*, 2016, **93**, 85142.

57 V. Stevanović, S. Lany, X. Zhang and A. Zunger, Correcting density functional theory for accurate predictions of compound enthalpies of formation: Fitted elemental-phase reference energies, *Phys. Rev. B: Condens. Matter Mater. Phys.*, 2012, **85**, 115104.

58 D.-J. Xue, Y. Hou, S.-C. Liu, M. Wei, B. Chen, Z. Huang, Z. Li, B. Sun, A. H. Proppe, Y. Dong, M. I. Saidaminov, S. O. Kelley, J.-S. Hu and E. H. Sargent, Regulating strain in perovskite thin films through charge-transport layers, *Nat. Commun.*, 2020, **11**, 1514.

59 L. J. Ji, S. J. Sun, Y. Qin, K. Li and W. Li, Mechanical properties of hybrid organic-inorganic perovskites, *Coord. Chem. Rev.*, 2019, **391**, 15.

60 S. Sun, F. H. Isikgor, Z. Deng, F. Wei, G. Kieslich, P. D. Bristowe, J. Ouyang and A. K. Cheetham, Factors Influencing the Mechanical Properties of Formamidinium Lead Halides and Related Hybrid Perovskites, *ChemSusChem*, 2017, **10**, 3740.

61 M. A. Reyes-Martinez, A. L. Abdelhady, M. I. Saidaminov, D. Y. Chung, O. M. Bakr, M. G. Kanatzidis, W. O. Soboyejo and Y. L. Loo, Time-Dependent Mechanical Response of APbX3 (A=Cs, CH3NH3; X=I, Br) Single Crystals, *Adv. Mater.*, 2017, **29**, 1.

62 W. Travis, E. N. K. Glover, H. Bronstein, D. O. Scanlon and R. G. Palgrave, On the application of the tolerance factor to inorganic and hybrid halide perovskites: A revised system, *Chem. Sci.*, 2016, **7**, 4548.

63 R. D. Shannon, Revised effective ionic radii and systematic studies of interatomic distances in halides and chalcogenides, *Acta Crystallogr., Sect. A: Cryst. Phys., Diffr., Theor. Gen. Crystallogr.*, 1976, **32**, 751.

64 C. Li, X. Lu, W. Ding, L. Feng, Y. Gao and Z. Guo, Formability of ABX 3 (X=F, Cl, Br, I) halide perovskites, *Acta Crystallogr., Sect. B: Struct. Sci.*, 2008, **64**, 702.

65 A. Šimůnek and J. Vackář, Hardness of covalent and ionic crystals: First-principle calculations, *Phys. Rev. Lett.*, 2006, **96**, 5.

66 P. Sánchez-Palencia, G. García, J. C. Conesa, P. Wahnón and P. Palacios, Spinel-Type nitride compounds with improved features as solar cell absorbers, *Acta Mater.*, 2020, **197**, 316.

67 J. Yang, Q. Zhang, J. Xu, H. Liu, R. Qin, H. Zhai, S. Chen and M. Yuan, All-inorganic perovskite solar cells based on cspbibr2 and metal oxide transport layers with improved stability, *Nanomaterials*, 2019, **9**, 1666.

68 Y. Gupta, A. Palakkandy, S. V. Syrotyuk, K. Kumar and S. Arora, A Novel Route for Fabrication of Stable CsPbI 3 Perovskite Thin Film by Thermal Evaporation, *ChemistrySelect*, 2019, **4**, 5091.

69 F. Birch, Finite elastic strain of cubic crystals, *Phys. Rev.*, 1947, **71**, 809.

70 F. D. Murnaghan, The Compressibility of Media under Extreme Pressures, *Proc. Natl. Acad. Sci. U. S. A.*, 1944, **30**, 244.

71 Y. Le Page and P. Saxe, Symmetry-general least-squares extraction of elastic data for strained materials from ab initio calculations of stress, *Phys. Rev. B: Condens. Matter Mater. Phys.*, 2002, **65**, 104104.

72 M. De Jong, W. Chen, T. Angsten, A. Jain, R. Notestine, A. Gamst, M. Sluiter, C. K. Ande, S. Van Der Zwaag, J. J. Plata, C. Toher, S. Curtarolo, G. Ceder, K. A. Persson and M. Asta, Charting the complete elastic properties of inorganic crystalline compounds, *Sci. Data*, 2015, **2**, 1.

73 R. Hill, Related content The Elastic Behaviour of a Crystalline Aggregate, *Proc. Phys. Soc., London*, 1952, **65**, 349.

74 J. P. Perdew, A. Ruzsinszky, G. I. Csonka, O. A. Vydrov, G. E. Scuseria, L. A. Constantin, X. Zhou and K. Burke, Restoring the density-gradient expansion for exchange in solids and surfaces, *Phys. Rev. Lett.*, 2008, **100**, 1.

75 J. Sun, A. Ruzsinszky and J. Perdew, Strongly Constrained and Appropriately Normed Semilocal Density Functional, *Phys. Rev. Lett.*, 2015, **115**, 1.

76 S. Pramchu, A. P. Jaroenjittichai and Y. Laosiritaworn, Effects of bromine substitution for iodine on structural stability and phase transition of CsPbI3, *Appl. Surf. Sci.*, 2019, **496**, 1.

77 S. Dastidar, C. J. Hawley, A. D. Dillon, A. D. Gutierrez-Perez, J. E. Spanier and A. T. Fafarman, Quantitative Phase-Change Thermodynamics and Metastability of Perovskite-Phase Cesium Lead Iodide, *J. Phys. Chem. Lett.*, 2017, **8**, 1278.

78 I. Chung, J. H. Song, J. Im, J. Androulakis, C. D. Malliakas, H. Li, A. J. Freeman, J. T. Kenney and M. G. Kanatzidis, CsSnI 3: Semiconductor or metal? High electrical conductivity and strong near-infrared photoluminescence from a single material. High hole mobility and phase-transitions, *J. Am. Chem. Soc.*, 2012, **134**, 8579.

79 T. J. Whitcher, L. C. Gomes, D. Zhao, M. Bosman, X. Chi, Y. Wang, A. Carvalho, H. K. Hui, Q. Chang, M. B. H. Breese, A. H. Castro Neto, A. T. S. Wee, H. D. Sun, E. E. M. Chia and A. Rusydi, Dual phases of crystalline and electronic structures in the nanocrystalline perovskite $CsPbBr_3$, *NPG Asia Mater.*, 2019, **11**, 70.

80 S. Gupta, T. Bendikov, G. Hodes and D. Cahen, CsSnBr3, A Lead-Free Halide Perovskite for Long-Term Solar Cell Application: Insights on SnF2 Addition, *ACS Energy Lett.*, 2016, **1**, 1028.

81 D. Liu, W. Zha, Y. Guo and R. Sa, Insight into the improved phase stability of CsPbI3 from First-Principles Calculations, *ACS Omega*, 2020, **5**, 893.

82 Z. Wang, A. K. Baranwal, M. A. Kamarudin, Y. Kamata, C. H. Ng, M. Pandey, T. Ma and S. Hayase, Structured crystallization for efficient all-inorganic perovskite solar cells with high phase stability, *J. Mater. Chem. A*, 2019, **7**, 20390.

83 R. J. Sutton, M. R. Filip, A. A. Haghighirad, N. Sakai, B. Wenger, F. Giustino and H. J. Snaith, Cubic or Orthorhombic? Revealing the Crystal Structure of Metastable Black-Phase CsPbI3 by Theory and Experiment, *ACS Energy Lett.*, 2018, **3**, 1787.

84 D. Sabba, H. K. Mulmudi, R. R. Prabhakar, T. Krishnamoorthy, T. Baikie, P. P. Boix, S. Mhaisalkar and N. Mathews, Impact of anionic Br- substitution on open circuit voltage in lead free perovskite (CsSnI3-xBrx) solar cells, *J. Phys. Chem. C*, 2015, **119**, 1763.

85 R. Grau-Crespo, S. Hamad, C. R. A. Catlow and N. H. De Leeuw, Symmetry-adapted configurational modelling of fractional site occupancy in solids, *J. Phys.: Condens. Matter*, 2007, **19**, 256201.

86 D. M. Trots and S. V. Myagkota, High-temperature structural evolution of caesium and rubidium triiodoplumbates, *J. Phys. Chem. Solids*, 2008, **69**, 2520.

87 D. H. Fabini, G. Laurita, J. S. Bechtel, C. C. Stoumpos, H. A. Evans, A. G. Kontos, Y. S. Raptis, P. Falaras, A. Van Der Ven, M. G. Kanatzidis and R. Seshadri, Dynamic Stereochemical Activity of the Sn2+Lone Pair in Perovskite CsSnBr3, *J. Am. Chem. Soc.*, 2016, **138**, 11820.

88 A. Jain, S. P. Ong, G. Hautier, W. Chen, W. D. Richards, S. Dacek, S. Cholia, D. Gunter, D. Skinner, G. Ceder and K. A. Persson, Commentary: The materials project: A materials genome approach to accelerating materials innovation, *APL Mater.*, 2013, **1**, 011002.

89 T. Oku, Crystal structures of perovskite halide compounds used for solar cells, *Rev. Adv. Mater. Sci.*, 2020, **59**, 264.

90 S. F. Pugh, XCII. Relations between the elastic moduli and the plastic properties of polycrystalline pure metals, *London, Edinburgh Dublin Philos. Mag. J. Sci.*, 1954, **45**, 823.

91 R. P. Thompson and W. J. Clegg, Predicting whether a material is ductile or brittle, *Curr. Opin. Solid State Mater. Sci.*, 2018, **22**, 100.

92 A. Lamichhane and N. M. Ravindra, Isosymmetric compression of cubic halide perovskites ABX3 (A=K, Rb, Cs; B=Ge, Sn, Pb and X=Cl,Br,I)-influence of cation–anion exchange: a first principle study, *SN Appl. Sci.*, 2021, **3**, 153.

93 Y. Rakita, S. R. Cohen, N. K. Kedem, G. Hodes and D. Cahen, Mechanical properties of APbX3 (A=Cs or CH3NH3; X=i or Br) perovskite single crystals, *MRS Commun.*, 2015, **5**, 623.

94 M. Afsari, A. Boochani and M. Hantezadeh, Electronic, optical and elastic properties of cubic perovskite CsPbI3: Using first principles study, *Optik*, 2016, **127**, 11433.

95 M. A. Fadla, B. Bentria, T. Dahame and A. Benghia, First-principles investigation on the stability and material properties of all-inorganic cesium lead iodide perovskites CsPbI3 polymorphs, *Physica B: Condens. Matter*, 2020, **585**, 412118.

96 Q. Mahmood, M. Yaseen, M. Hassan, M. S. Rashid, I. Tlili and A. Laref, The first-principle study of mechanical, optoelectronic and thermoelectric properties of CsGeBr3 and CsSnBr3 perovskites, *Mater. Res. Express*, 2019, **6**, 045901.

97 Q. Mahmood, M. Hassan, M. Rashid, B. U. Haq and A. Laref, The systematic study of mechanical, thermoelectric and optical properties of lead based halides by first principle approach, *Physica B: Condens. Matter*, 2019, **571**, 87.

98 H. Jing, R. Sa and G. Xu, Tuning electronic and optical properties of CsPbI3 by applying strain: A first-principles theoretical study, *Chem. Phys. Lett.*, 2019, **732**, 4.

INORGANIC CHEMISTRY
FRONTIERS

CHINESE CHEMICAL SOCIETY
ROYAL SOCIETY OF CHEMISTRY

RESEARCH ARTICLE

Cite this: *Inorg. Chem. Front.*, 2022, **9**, 1337

Cation substitution effects on the structural, electronic and sun-light absorption features of all-inorganic halide perovskites†

Pablo Sánchez-Palencia, [a,b] Gregorio García, *[a,b] Perla Wahnón [a,b] and Pablo Palacios [a,c]

Received 15th December 2021,
Accepted 18th February 2022

DOI: 10.1039/d1qi01553b

rsc.li/frontiers-inorganic

All-inorganic perovskites (such as $CsPbI_3$) are emerging as new candidates for photovoltaic applications. Unfortunately, this class of materials present two important weaknesses in their way to commercialization: poor stability and toxicity. This paper explores the possibility of lessening both stability and toxicity related problems, as well as obtaining improved photovoltaic efficiencies through the propitious fine-tuning of the chemical composition. Therefore, a systematic *ab initio* study of the family of all-inorganic perovskites with the general formula $Rb_aCs_{1-a}Sn_bPb_{1-b}I_2Br$ (a = 0–0.125 and b = 0–1) is here presented. Our results provide a complete description on the connections between the chemical composition, crystal structure, intrinsic stability, electronic properties, and absorption features, pointing out that all-inorganic $Rb_aCs_{1-a}Sn_bPb_{1-b}I_2Br$ (a = 0.125 and 1 > b > 0.5) perovskites would be adequate candidates for photovoltaic applications with improved stability and reduced Pb concentration.

Introduction

Perovskites became a mandatory line of research in any laboratory with interests in photovoltaic energy for a few years now, with more than 3000 research articles per year since 2017 (data from the Web of Science with the keyword perovskite solar cell). Thanks to all the research devoted to these materials that the promising 3% efficiency presented barely 15 years ago turned into a really impressing power conversion efficiency (PCE) of 25.5% (29.5% when used in tandem configuration with Si cells) in record time.[1–6] These high efficiencies were initially reported for the organic–inorganic hybrid methylammonium lead iodide (MAPI) perovskite. During the last years, the vast majority of the efficiency records for organic–inorganic hybrid perovskites have been obtained for MAPI and formamidinium lead iodide (FAPI) perovskites or their mixtures. Thanks to their outstanding properties, such as a very adequate direct bandgap,[7,8] a high absorption coefficient,[9,10] superior ambipolar charge mobility and long charge diffusion length[11–13] and a small exciton binding energy,[14–16] perovskites are attracting great interest, leading the way for the new generation of solar cells, cheaper and at least as efficient as the present leader technology, silicon solar cells. Nevertheless, besides all their strengths, organic–inorganic perovskites, particularly MAPI and FAPI, also present some important weaknesses, two of which are especially crucial in their way to commercialization: their poor stability and toxicity.[17–19] Both stability and toxicity related problems can be solved through the adequate modification of the chemical composition.

There are several mechanisms by which perovskites generally suffer instability problems. The most common of them are hydration, oxidation, polymorphic transition and direct decomposition.[20–23] Besides intrinsic instability of the corresponding compound, these mechanisms can be induced by different agents including UV light, heat, oxygen and moisture. As a result of all these issues, perovskites present the highest lifetimes of 10 000/1000 h in storage/under illumination in tests,[24] far below necessities to compete against silicon technology, which is used in devices that last for 25 years or even more.[19] This way, those mechanisms of degradation need to be addressed in depth without delay. Looking at top-performers MAPI and FAPI, one of their main problems is the weak bond between the organic cations and the PbI_6 octahedra.[17,25] The different degrees of freedom of rotational and translational motion of the organic cation provoke ion migration or phase transitions that modify the properties of the

[a]*Instituto de Energía Solar, ETSI Telecomunicación, Universidad Politécnica de Madrid, Ciudad Universitaria, s/n, 28040 Madrid, Spain. E-mail: g.garcia@upm.es*
[b]*Departamento de Tecnología Fotónica y Bioingeniería, ETSI Telecomunicación, Universidad Politécnica de Madrid, Ciudad Universitaria, s/n, 28040 Madrid, Spain*
[c]*Departamento de Física Aplicada a las Ingenierías Aeronáutica y Naval. ETSI Aeronáutica y del Espacio, Universidad Politécnica de Madrid, Pz. Cardenal Cisneros, 3, 28040 Madrid, Spain*

†Electronic supplementary information (ESI) available. See DOI: 10.1039/d1qi01553b

compounds.[26–29] Organic cations are also the most affected under moisture conditions due to their high hygroscopicity.[30] For this reason, latest trends point towards substitution of the organic molecules with inorganic cations, trying to solve these problems.[31–35] In particular, the partial introduction of Cs substituting methylammonium or the corresponding organic molecules was initially studied, resulting in slightly better stabilities.[36,37] Most recently, the focus has turned towards total replacement of the organic molecule, leading to fully inorganic perovskites,[38] with $CsPbI_3$ gathering much attention.[39–42] Unfortunately, all-inorganic $CsPbI_3$ perovskite presents spontaneous phase transition from the photoactive perovskite black α-phase to the light-inactive yellow δ-phase, mainly because of distortions of the structure caused by the small size of the cesium atoms to hold the PbI_6 octahedra.[43,44] In order to overcome this issue, partial compositions of different halides have been extendedly studied,[39,45–49] with different compromise solutions between stability and suitable bandgaps for photovoltaic applications, considering that smaller halides result in compounds with larger bandgaps. Among those solutions outstands the $CsPbI_2Br$ perovskite, which exhibits an adequate bandgap but also phase stability at room temperature, thanks to a lower phase transition temperature with the bromine addition.[45,50–54] In this line of using chemical composition as a tool to solve stability problems, many other options, aside from those previously mentioned, have been studied and tested, with a myriad of different elements at different levels of concentration.[43,55–63] Among them, the presence of small rubidium concentrations (around 0.05–0.1) has been proposed to improve the stability of cesium perovskites, passivating grain boundaries and hardly changing bandgap values.[64–67]

Toxicity problems are linked to the presence of lead atoms. Replacing this element seems a logic solution.[68–75] However, lead *s* and p-states comprise and shape the valence band maximum and conduction band minimum in perovskites,[76] therefore being responsible for the high PCE values, because of which it is difficult to get rid of this element without jeopardizing efficiency. Structural variations of the simple perovskite, like double perovskites or even more complex structures have been suggested as an alternative to lead-based perovskites; however, they present indirect bandgaps and very low mobilities of charge carriers, leading to PCEs not exceeding 3%.[69,77–79] Better results in terms of PCE have been presented with tin perovskites, more similar to lead perovskites than other options although with little worse stability, mainly because of issues related to Sn^{2+} oxidation.[80,81] Fighting with this issue, it has been reported that Rb introduction can also help in reducing significantly formation of Sn^{4+} vacancies.[66] For the case of pure tin perovskites PCEs of 14% have been reached (10% for all-inorganic perovskites), while for mixed lead-tin the rise is up to 21% for the moment.[82–85]

Following lines of design for new all-inorganic perovskite solar cells with improved efficiency and stability and lower lead-related toxicity issues, compounds with different Pb/Sn ratios, as well as Rb-doped compounds, *i.e.*, $Rb_aCs_{1-a}Sn_bPb_{1-b}I_2Br$ (a = 0–0.125; b = 0–1), are explored by Density Functional Theory (DFT).[86,87] The usefulness of a computational analysis through the DFT method is noticeable, acting as a roadmap of properties for experimentalists, which has much more difficulties in covering wide spaces of chemical composition with different concentration rates, in terms of resources, time and cost of both.[68] Information on intrinsic stability and accurate description of the electronic structure, and sun-light absorption features are presented.

Computational details

The step-by-step procedure to conduct this analysis consists of three levels of DFT[86,87] and beyond DFT calculations. First of all, a structure optimization of all the compounds, to relax atomic forces and total energies within a tolerance of 0.01 eV $Å^{-1}$ and 10^{-5} eV, has been performed, followed by a static calculation of the electronic structure with a very dense grid of *k*-points to fully describe the reciprocal space. For the structural relaxation step, the PBEsol functional,[88] with higher accuracies presented for this task when used in solids, has been used in all the cases, while the standard PBE functional[89] has been chosen for the obtention of electronic structure in static calculations. Regarding *k*-point meshes, Γ-centered Monkhorst–Pack grids[90] of 8 × 8 × 8 and 12 × 12 × 12 points have been applied to these steps, respectively.

Due to the widely known underestimation of the bandgap values of the GGA level of theory, a subsequent step or level of calculation is required to obtain accurate electronic structures and their dependent properties, like the bandgaps and the dielectric constants. With this purpose, beyond DFT level calculations using the Hubbard model for the electron correlation, widely known as the DFT+*U* method,[91,92] have been performed. Other approximations, like different *GW* calculations based on many body perturbation theory,[93] the hybrid HSE06 functional[94] or a combination of both of them have also been tested. In fact, as reported in previous works on the matter, *GW* presents very precise results when used on top of PBE relaxed structures when compared to experimental values of inorganic perovskites,[95,96] excluding finite-temperature calculations to account for thermal effects, which are far more expensive in terms of computational cost and for that reason out of the scope of this work. Nevertheless, all those methods dramatically fail when used on top of structures relaxed with PBEsol (which in turn are more precise than those obtained with PBE), especially for those compounds that show metallic or almost metallic nature when calculated with PBE. Inclusion of the spin–orbit coupling (SOC) effect[97] in the calculations has also been tested and properly discussed in the results section of this work. All the calculations proposed here have been performed with the projector-augmented wave scheme as implemented in the Vienna *Ab initio* Simulation Package (VASP).[98–100]

All-inorganic $Rb_aCs_{1-a}Sn_bPb_{1-b}I_2Br$ perovskites with different partial concentrations of the IV-group cations (a = 0.0

and 0.125; b = 0.0, 0.125, 0.25, 0.5, 0.75, 0.875, and 1.0) have been studied in this work. The model system of $Rb_aCs_{1-a}Sn_bPb_{1-b}I_2Br$ perovskites was built starting from the 2 × 2 × 2 supercell of $CsPbI_3$ with 40 atoms. Additionally, the effect of lower Rb concentrations (a = 0.0625) on the bandgap has been also studied using bigger 4 × 2 × 2 supercells with 80 atoms. Only cubic perovskite structures have been considered for this work, as those with solar application considering non-perovskite phases exhibit larger bandgaps with no interest for this work.[101,102] Configuration of the IV-group and Rb atoms for the different concentrations has been defined by looking for the highest space group symmetries, using the combinatorial methodology implemented in the SOD (Site Occupancy Disorder) program.[103]

Results and discussion

The study of all-inorganic $Rb_aCs_{1-a}Sn_bPb_{1-b}I_2Br$ perovskites is divided into three sections aimed at assessing their main structural and electronic features as a function of the chemical composition. Firstly, in an analysis of the most important structural parameters, distortions and intrinsic stabilities are given. The second section is devoted to selecting an adequate DFT method, which should provide accurate electronic band structures and absorption properties bearing in mind a good compromise between accuracy and computational effort. Finally, electronic structure properties and absorption coefficients are assessed.

Structural and thermodynamic parameters

A detailed structural analysis to assess the structure distortion (*i.e.*, changes in the unit cell structures when Cs and/or Pb are atoms are replaced in relation to the pristine compound, $CsPbI_2Br$) can throw relevant information on intrinsic stability. Lattice constants, bond distances, inner angles of PbI_6 octahedra – or BX_6, generalized for different chemical compositions – and Goldschmidt's tolerance factor offer an overview of the perovskite cubic phase predominance over other structures like orthorhombic, the crystal quality or intrinsic stability, paying special attention to tilting or rotation of the octahedra, which we already know leads to deterioration of conductivity properties among others.[26,28] Also, total energies from static calculations allow for obtaining formation enthalpies, considering at least fundamental elements, binary compounds from typical decomposition pathways and pure ternary perovskites to account for phase segregation.

To gain some insight into the structure of all-inorganic perovskites, the $CsPbX_3$ perovskite structure is depicted in Fig. 1, paying special attention to the bond-generated octahedral configuration (BX_6 and XCs_4B_2), whose proportions and dimensions are related to the structural stability. As seen for $CsPbI_2Br$, the pseudo-cubic structure comes from the combination of two halogens in the X position, where bromines occupy opposite corners in the octahedra along one same direction with a consequent shortening of that lattice vector.

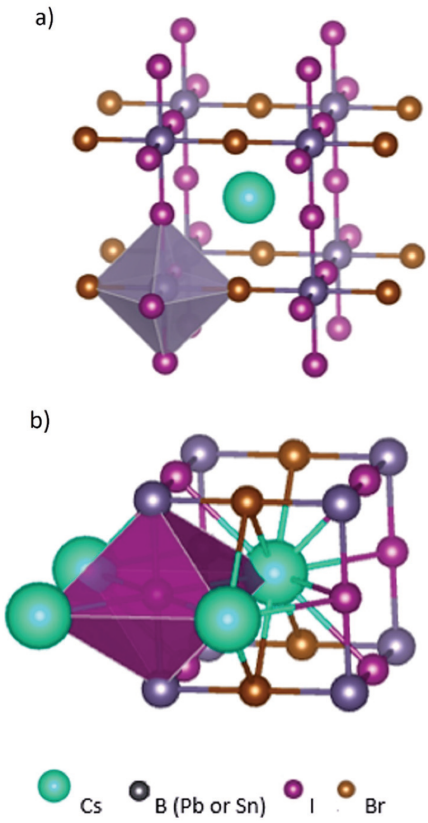

Fig. 1 Structure of a $CsPbI_2Br$ perovskite crystal with the different octahedra generated by atom bonding highlighted: (a) BX_6 octahedron and (b) XCs_4B_2 octahedron.

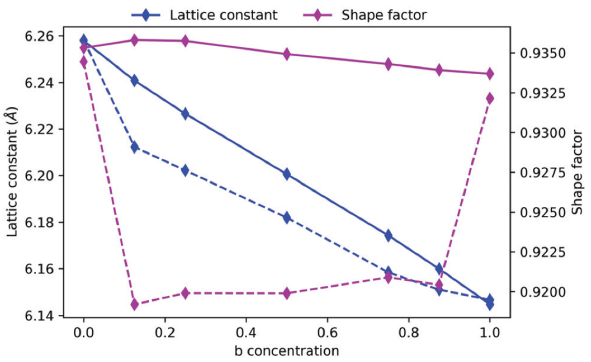

Fig. 2 Lattice constant (blue lines) and shape factor (purple lines) variations as a function of the chemical composition. Continuous lines correspond to $CsSn_bPb_{1-b}I_2Br$ compounds, while dashed lines correspond to $Rb_{0.125}Cs_{0.875}Sn_bPb_{1-b}I_2Br$.

First of all, the size and shape of the pseudo-cubic cells corresponding to the perovskite structure for the different compositions are presented in Fig. 2, where the main lattice constant and shape factor are depicted. The ratio between that shor-

tened vector modulus and that of the other identical two is what here called the shape factor, which measures deviation from that perfect cubic shape. In all the studied cases, those two non-shortened lattice vectors remain equal even after relaxation. Also, orthogonality between lattice vectors of the unit cell is perfectly preserved, with the only exceptions of Rb-doped compounds with partial concentrations of Pb and Sn other than 0.5 ($Rb_{0.125}Cs_{0.875}Sn_bPb_{1-b}I_2Br$ with b = 0.125, 0.25, 0.75, or 0.875), where maximum deviations of 0.23° are observed. This way unit cell angles are not considered as a relevant parameter here. From Fig. 2, it can be observed that the lattice constant decreases linearly in coherence with the size of the divalent cations with the concentration of tin and lead. On the contrary, for the compounds with rubidium a significant reduction of the unit cell size is observed, except for the quaternary cases (b = 0 or b = 1), in which no substantial effect is noticed. That reduction is more acute in comparison to compounds without rubidium for higher concentrations of lead.

Meanwhile, shape factor hardly changes with b concentration for compounds without rubidium and for those with rubidium an additional shortening occurs in the same compounds where a reduction of the lattice parameter occurs, leading to smaller volumes of the cells in comparison. The same trend occurs again with introduction of tin softening that reduction, as we can see comparing the volumes of the compounds with the same b concentration with and without rubidium, where volume ratios of 0.9688 and 0.9813 are observed for b equal to 0.125 and 0.875 respectively, and intermediate values following the trend too.

In those compounds where both Cs and Pb ions are partially replaced, the variety of distance values between the same kind of two ions (Cs–X, Rb–X, Pb–X, and Sn–X, where X = I or Br) due to different surrounding environments is a good indicator of the crystal structure distortion. Fig. 3 presents average distances between different ions for all the compounds, as well as standard deviations from those mean values. Both AX (Fig. 3a) and BX (Fig. 3b) distances confirm that there are no distortions of the perovskite structure besides the shortening along the Br string direction for compounds without rubidium. Note that both $CsPbI_2Br$ and $CsSnI_2Br$ present a well-defined perovskite structure, with the exception of the shortened lattice vector on the Br string direction. Introduction of low rates of Rb (1/8 of total monovalent cations) is not enough to distort PbI_4Br_2 octahedra and the cells are this way able to dilute the effect of the small size of the Rb atom and preserve its shape. This fact can be noticed mainly from zero standard deviations among different distances presented. Pure tin and lead structures with rubidium present almost identical distances to their equivalents without rubidium, which means no substantial distortions either, as confirmed from lattice parameters and inner angles. For all these compounds the larger standard deviation is 0.01 Å, which represents a variation below 0.4% of the total bond distance. Regarding the remaining distorted structures (those with rubidium and b = 0.125, 0.25, 0.5, 0.75, and 0.875), great differences between Cs–X and Rb–X are good evidence of unbalanced structures, apart from

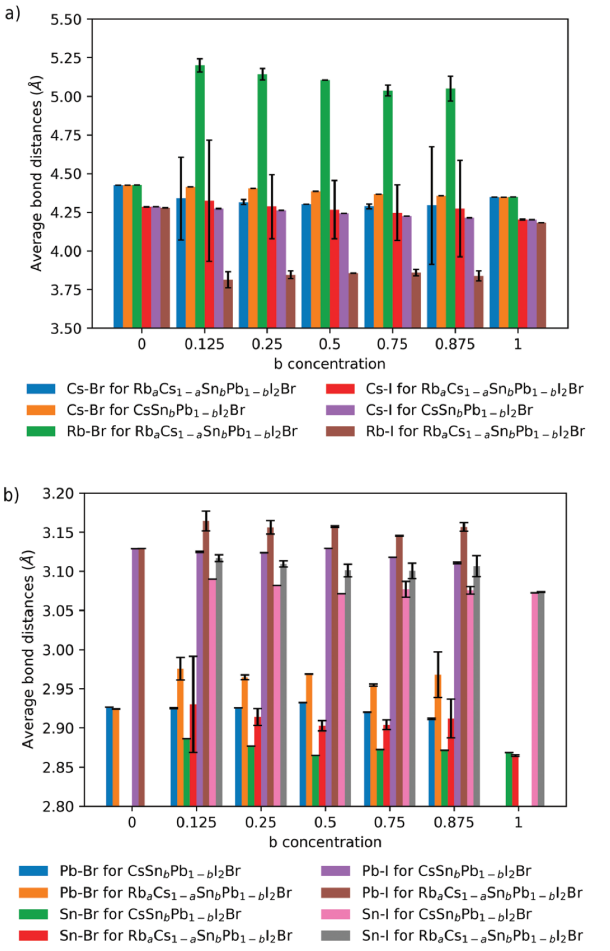

Fig. 3 Average bond distances of the different cations and anions in the cell, including standard deviations grouped in (a) AX distances and (b) BX distances.

larger standard deviations from mean distances than the previous cases. Compounds with b concentrations equal to 0.125 and 0.875 are those with more accused distortions, especially for Sn–Br, Cs–I and mostly for Cs–Br distances, where standard deviations of 0.26 and 0.38 Å respectively are reached, more than 25 times higher than those for the intermediate structures with b equal to 0.25, 0.5 and 0.75. A fact that is worth noticing is that despite the smaller size of the distorted cells, the BX_6 octahedra increase their size in these distorted structures, as can be seen in their longer BX distances. This could be one possible reason for deviations from trends in their optical properties that will be explained later.

In Fig. 4 the different angles defined by X–B–X bonds are presented. For simplicity, only deviations from original right and straight angles are shown and just for the perovskites with rubidium, as those without it present no deviations at all from the orthogonal directions. This way four different angles are

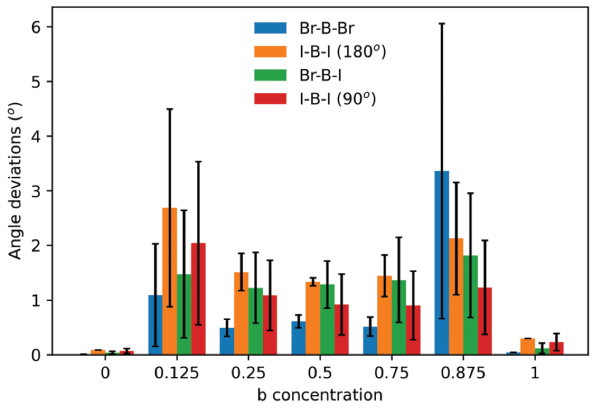

Fig. 4 Averaged inner angle deviations from ideal right and straight angles within the BX_6 octahedra for $Rb_{0.125}Cs_{0.875}Sn_bPb_{1-b}I_2Br$ perovskites, including standard deviations.

presented: Br–B–Br which ideally forms 180° angles, Br–B–I defining 90° angles and theoretically coplanar I–B–I angles divided in straight and right angles. We opted for presenting deviations from right angles in absolute values, to avoid compensation for means of zero, and consequently deviations from straight angles are presented in positive for convenience when looking at the graph. One more time, structures without rubidium present perfectly ideal values of 90° and 180° for every inner angle, while for $Rb_{0.125}Cs_{0.875}SnI_2Br$ and $Rb_{0.125}Cs_{0.875}PbI_2Br$ maximum deviations of 0.3° take place. In contrast, quinary compounds ($Rb_{0.125}Cs_{0.875}Sn_bPb_{1-b}I_2Br$ for b = 0.125, 0.25, 0.5, 0.75 and 0.875) present maximum deviations up to 6° for the two more distorted compounds (those with a 1 to 7 proportion of divalent cations) and up to 2° for the other three compounds, which is still a quite high value. To emphasize distortion in those first two compounds is enough to look at the enormous variability, represented by the standard deviation, among all the angles which basically means that almost every octahedron is different from the next one. The minimum and maximum standard deviations for those two compounds are 0.86° and 2.70°, with the maximum for the other three compounds being 0.78°.

The Goldschmidt tolerance factor (t) is widely used to assess the stability within this cubic phase and the possibility of a phase transition because of structure distortion,[104,105] which is defined as

$$t = \frac{r_A + r_X}{\sqrt{2}(r_B + r_X)} \quad (1)$$

where r_A, r_B and r_X correspond to the elemental radii of the ions occupying the corresponding position in the perovskite structure as previously named, considering weighted radii when needed because of mixed cations or anions (*i.e.*, $r_X = 1/3{\cdot}r_{Br} + 2/3{\cdot}r_I$, $r_A = a{\cdot}r_{Rb} + (1-a){\cdot}r_{Cs}$ and $r_B = b{\cdot}r_{Sn} + (1-b){\cdot}r_{Pb}$).

As stated in the scientific literature,[105] those compounds with Goldschmidt values between 0.8 and 1 are plausible to exist in perovskite form, thanks to a well-balanced size of their atoms which allows for holding the BX_6 octahedra without important distortions that subsequently lead to a phase transition. As expected, Goldschmidt parameter shows linear variations with composition, as it is defined exclusively by the radii of the atoms occupying different positions in the perovskite structure, weighted when more than one element occupies equivalent positions. Values of all the compounds studied here fall within that range, with the minimum and maximum values being 0.850 and 0.887, corresponding to $Rb_{0.125}Cs_{0.875}PbI_2Br$ and $CsSnI_2Br$ respectively (see Fig. 5).

Finally, the intrinsic stability of studied compounds has been also assessed from a thermodynamic perspective through their formation enthalpies. Both formation enthalpies compared to fundamental elements (ΔH_f) and binary compounds (ΔH_d), according to the standard route from minimal energy binary compounds, have been defined as follows:

$$\begin{aligned}\Delta H_f = {} & E_{tot}\left[Cs_{1-a}Rb_aPb_{1-b}Sn_bI_2Br\right] \\ & - \{(1-a)\cdot\mu^0_{Cs} + a\cdot\mu^0_{Rb} \\ & + (1-b)\cdot\mu^0_{Pb} + b\cdot\mu^0_{Sn} + 2\cdot\mu^0_{I} + \mu^0_{Br}\}\end{aligned} \quad (2)$$

$$\begin{aligned}\Delta H_d = {} & E_{tot}[Cs_{1-a}Rb_aPb_{1-b}Sn_bI_2Br] \\ & - \{(1-a)\cdot E_{tot}[CsBr] + a\cdot E_{tot}[RbBr] \\ & + (1-b)\cdot E_{tot}[PbI_2] + b\cdot E_{tot}[SnI_2]\}\end{aligned} \quad (3)$$

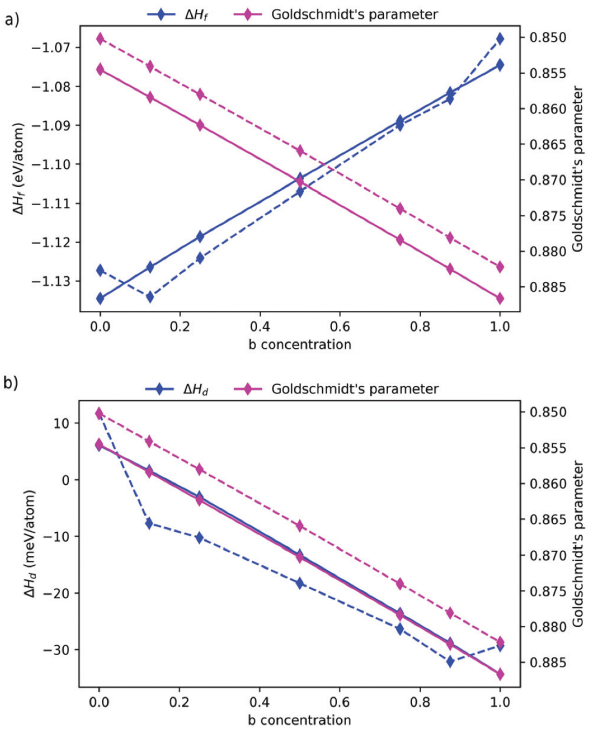

Fig. 5 Goldschmidt tolerance factor (purple lines) and formation enthalpies (blue lines) *vs.* (a) fundamental elements and (b) binary compounds. Continuous lines correspond to $CsSn_bPb_{1-b}I_2Br$ compounds, while dashed lines correspond to $Rb_{0.125}Cs_{0.875}Sn_bPb_{1-b}I_2Br$.

where $E_{tot}[M]$ and μ_i^0 stand for the total energy of M (M = $Rb_aCs_{1-a}Sn_bPb_{1-b}I_2Br$, CsBr, RbBr, PbI_2, and SnI_2) and chemical potential of constituent element i (i = Rb, Cs, Pb, Sn, I, and Br), *i.e.*, the total energy per atom in its corresponding bulk phase, respectively.

Fig. 5a and b display ΔH_s and ΔH_d, respectively, in both cases contrasted to Goldschmidt tolerance factor displayed in the right axis. Fundamental element enthalpies are below −1 eV per atom for all the compounds. In general, negative ΔH_f values determine the range of chemical potential within which the studied material would be thermodynamically stable, being negative values an essential although not sufficient on itself requirement for synthesizability of the materials. In this case, this metastability criteria is accomplished by far, proving the stability of the perovskite structure and the suitability of the elements chosen, being compounds with lead those with lowest values. Except for $CsPbI_2Br$ and $CsSnI_2Br$, the substitutional doping with Rb leads to slightly lower ΔH_f values. Another limit to be considered for the compounds to be stable would be also negative values of ΔH_d. In this case, the same linear trend as the one observed for the Goldschmidt parameter is also observed for all the studied perovskites without rubidium, while for those with Rb linearity disappears because of the distortion of the structure. Introduction of Sn improves the stability *versus* these binary compounds as indicated by lower values. This way, the maximum value is observed for $Rb_{0.125}Cs_{0.875}PbI_2Br$ with 11.69 meV per atom and the minimum of −34.31 meV per atom is for $CsSnI_2Br$, slightly lower than that of $Rb_{0.125}Cs_{0.875}Sn_{0.875}Pb_{0.125}I_2Br$. Positive values indicate certain leaning to decomposition through that pathway, although as we previously commented all the compounds fall within the metastability limit and those with positive values are reasonably below 15 meV per atoms, which is not higher enough to discard them for synthesizability. When comparing compounds with and without Rb, higher formation enthalpies are observed for pure tin and pure lead compounds where there is no significant distortion of the structure, but when distortion takes place the opposite happens. This way, it's very interesting to see that distorted structures, as previously catalogued, are counterintuitively those with more negative values and therefore those with less probabilities to decompose this way. Paying attention to the comparison between both parameters, Fig. 5b shows clearly that Goldschmidt parameter results in a very good descriptor of thermodynamic stability, as trends of both parameters perfectly match for non-distorted compounds, but fail at the time of describing those structures farthest from the canonical perovskite structure.

DFT methods for electronic structures

One of the most important properties when evaluating the photovoltaic potential of a material is its bandgap, because it is the main parameter which defines its absorptivity of the solar light, which in turn determines PCE together with mobility and recombination. Besides bandgap values, the type of bandgap, direct or indirect, has also a direct impact on absorption, mobility and recombination, being this way of huge importance. For the case of all the compounds studied within this work, bandgaps are in all cases direct, thus increasing absorption.

To obtain precise bandgaps of all the studied compounds, considering underestimation associated with GGA calculations, different methods have been tested as previously commented (see the Computational details section). Those methods have been preliminarily tested in quaternary compounds $CsPbI_2Br$ and $CsSnI_2Br$, from which we have experimental bandgap values,[54,72] as well as for $CsSn_{0.5}Pb_{0.5}I_2Br$, to check also a compound with mixed cations in the B position. Bandgap values of these compounds and for the different methods tested are presented in Table 1. All the tested methods fail to overcome the initial underestimation from PBE. As seen in Table 1 for $CsSnI_2Br$, the initial guess from the PBE functional shows a metallic behaviour which cannot be corrected in any subsequent calculation with *GW* approximation nor the hybrid functional with an error of at least 0.97 eV. Despite not knowing previous values for $CsSn_{0.5}Pb_{0.5}I_2Br$, a bandgap somewhere between the values of

Table 1 Bandgap values with the different theoretical methods tested compared to experimental values

	$CsPbI_2Br$	$CsSn_{0.5}Pb_{0.5}I_2Br$	$CsSnI_2Br$
PBE	1.26	0.66	0.10
G_0W_0	1.79	0.95	0.13
GW_0	1.86	1.03	0.17
HSE06	1.73	1.04	0.40
HSE06 + G_0W_0	2.22	1.21	0.35
Experimental	1.91[a]	—	1.37[b]

[a] Experimental value taken from ref. 54. [b] Experimental value taken from ref. 72.

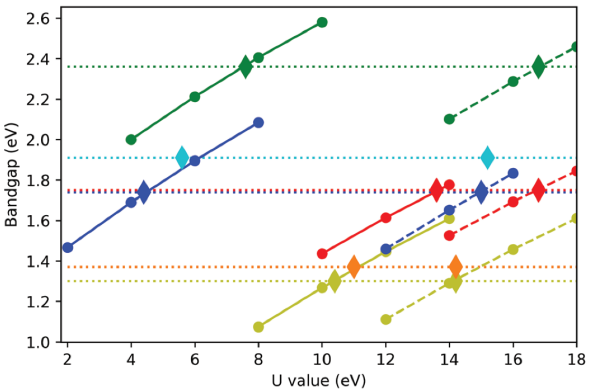

Fig. 6 Calculated bandgap using PBE+*U* (continuous lines) and PBE+*U*+SOC (dashed lines) for $CsPbI_3$ (blue), $CsPbBr_3$ (green), $CsSnI_3$ (yellow), $CsSnBr_3$ (red), $CsPbI_2Br$ (cyan) and $CsSnI_2Br$ (orange). Horizontal dotted lines stand for experimental bandgap values (taken from ref. 32, 54, 72 and 111–113); diamonds signal final values used for each compound.

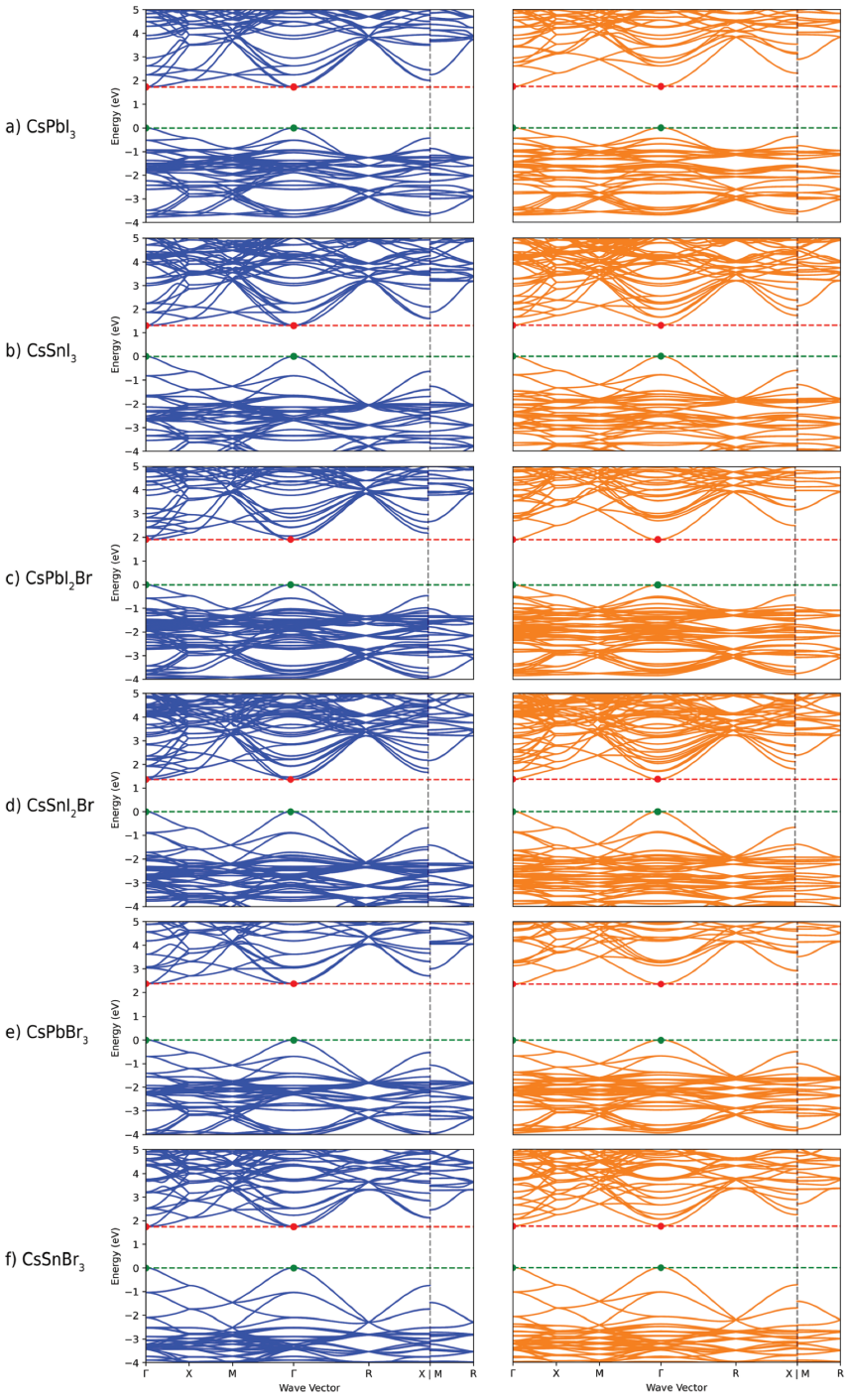

Fig. 7 Electronic band structures calculated using PBE+*U* (blue) and PBE+*U*+SOC (orange). *U* values of 5.6/11 eV for Pb/Sn without SOC and 15.2/14.2 when SOC is used. The zero of energy was set at the Fermi level energy. Horizontal dashed lines corresponded to conduction band minimum (red) and valence band maximum (green) energies calculated at the Γ-point.

the other two compounds should be expected, as although could not be linear the introduction of tin depicts a descent trend in the gap. Nevertheless, the highest value obtained is 0.16 eV lower than the experimental value of $CsSnI_2Br$. In the case of $CsPbI_2Br$ an acceptable underestimation of 0.05 eV is achieved with the GW_0 calculation, even though it could not be considered very precise to obtain accurate optical absorption spectra. The inclusion of the SOC would also tend to reduce bandgaps even more when separating degenerate states in the valence band.[106–108] Thus, its inclusion has been discarded. This way PBE+U turns out to be the only available solution to obtain accurate electronic structure results.

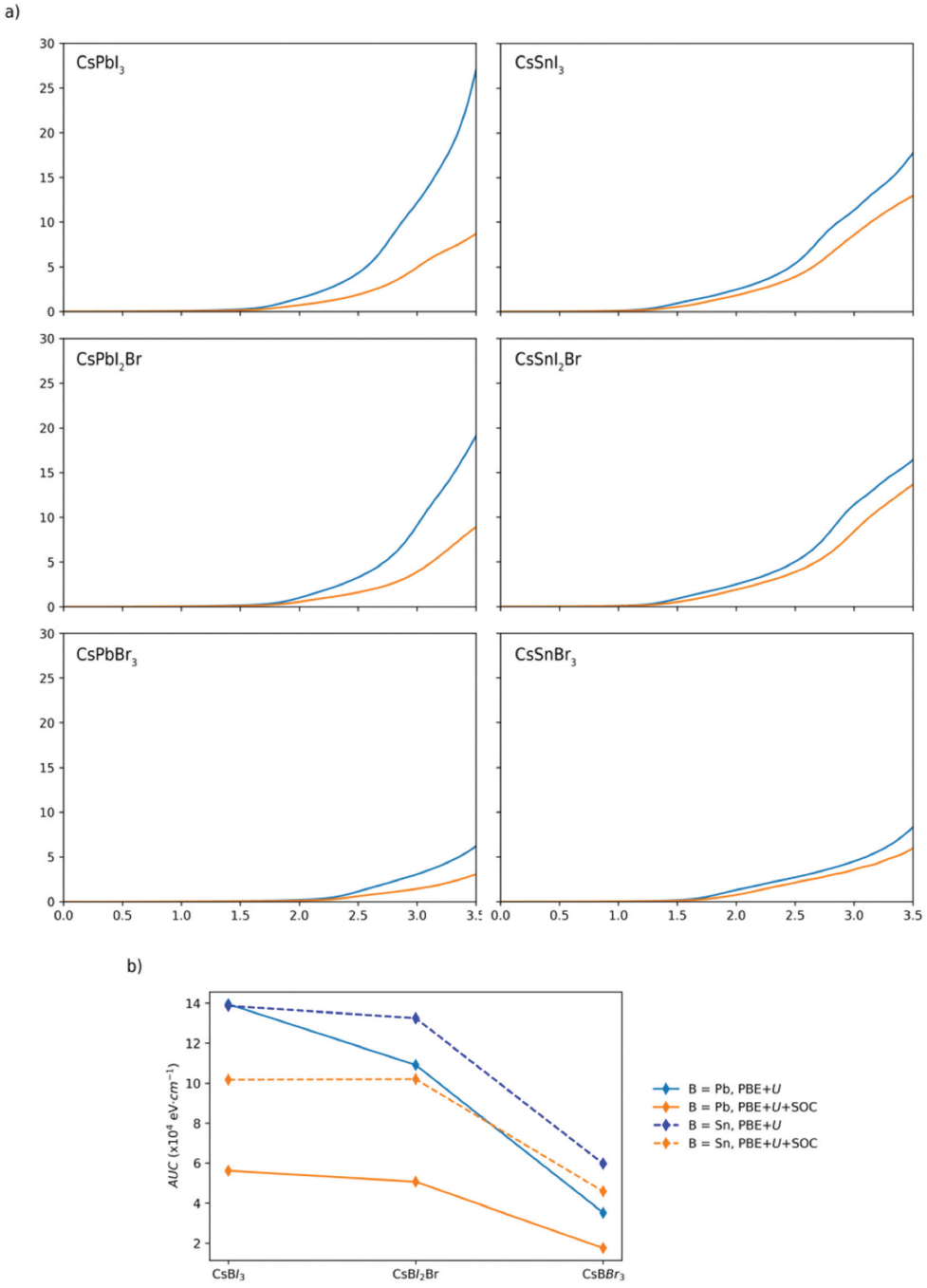

Fig. 8 (a) Calculated absorption coefficients with PBE+*U* (blue lines) and PBE+*U*+SOC (orange lines); (b) area under the curve (AUC) for the absorption coefficients. *U* values of 5.6/11 eV for Pb/Sn without SOC and 15.2/14.2 when SOC is used.

Finally for PBE+U, different U values have also been checked to obtain experimental bandgaps of the previous test compounds, but also of ternary perovskites with the anions (I and Br) and cations (Pb and Sn) studied here (see Fig. 6). Taking as a frame of reference the two compounds with only one divalent cation and with the relative concentration of halides studied here, $CsPbI_2Br$ and $CsSnI_2Br$, experimental values of the bandgap have been achieved with values of 5.6 and 11 eV applied to p-type orbitals of Pb and Sn respectively, and thus those have been chosen for the rest of the compounds with I_2Br concentration in the anion positions.

SOC effect inclusion. As stated before, PBE+U turned out to be the only available solution to present accurate electronic structure results. However, due to the presence of heavy atoms (Pb), electronic structure calculations with SOC should be carried out, *i.e.*, PBE+U+SOC. This method was tested for ternary compounds ($CsBX_3$, B = Pb and Sn; X = I and Br), quaternary ($CsBI_2Br$) and those with mixed cations at the B position ($CsSn_{0.5}Pb_{0.5}I_2Br$). For comparison purposes and seeking to compensate for the narrowing effect of SOC inclusion in the bandgap value, higher values of U have been used to obtain the same bandgap values as when SOC is not applied. This way, U values increase to 15.2 and 14.2 eV for Pb and Sn atoms, respectively, when the SOC effect is added (in comparison with the 5.6 and 11 eV in the absence of SOC). Bandgap value trends with some of the U-values tested for the different compounds are presented in Fig. 6.

Band structures of the reference compounds are depicted in Fig. 7, with a comparison side to side between calculations with and without the SOC effect. In those comparisons, the effect of SOC on the VB and CB of the compounds can be clearly seen. In all of them, p-type states of the cation, located near the CB minima, split in two branches pushing all but one states to higher energies. That way the CB is even less dense in the cases of the SOC effect included, which will be seen also in the absorption spectra in the form of a decrease of the absorption coefficient. On the contrary, VB states are a bit more compressed than without SOC, mitigating to some extent that effect, which is perfectly noticeable in compounds with higher concentration of Pb and slighter in those with more Sn.

As seen, accurate bandgap values can be easily achieved through an adequate selection of U values over p-type states of the B cation, regardless if SOC is included or not. In addition, the effects of SOC have been also checked for absorption coefficients. Fig. 8 shows a comparison of the calculated absorption coefficients with and without the SOC methodology. As can be seen, since the bandgap is accurately obtained by fine-tuning U values, the absorption coefficient yields a similar profile for both PBE+U and PBE+U+SOC methods, wherein the absorption edge starts to increase from the bandgap value. The main difference upon SOC inclusion is noted for the total absorption, which has been quantified through the area under the curve (AUC), that defines the integral of a curve that describes the absorption as a function of the energy. Fig. 8b displays AUC values calculated with PBE+U and PBE+U+SOC methods. As seen in Fig. 8b, the substitution of Pb by Sn leads to higher AUC values. If comparing differences between results with and without SOC for the compounds with lead and for the compounds with tin, it can be seen that SOC has a bigger impact for those compounds with B = Pb. Nonetheless, both PBE+U and PBE+U+SOC methods yield the same trend as a function of the chemical composition. Being one of the goals of this work to offer alternatives to lead for perovskite, as we increase the concentration of Sn in the compounds the use of SOC will have less and less meaning. Therefore, PBE+U is an adequate method to yield accurate bandgap values and related properties, such as absorption coefficients. With all these results and taking into account the increase of resources demanded by SOC included calculations, around 3 times more memory and 5–10 times in terms of computing hours according to our results, the decision to not include the SOC effect in our calculations was made, also considering that a respectable number of compounds are being studied.

Electronic structure analysis and absorption properties

Fig. 9 depicts bandgap values for $Rb_aCs_{1-a}Sn_bPb_{1-b}I_2Br$ perovskites studied here. Its similarity to previously presented figures like those for formation enthalpy *vs.* binary precursors (Fig. 5b) and lattice parameter (Fig. 2) can be seen clearly, meaning a strong correlation of these bandgap values with structure distortion as well. An almost linear trend is observed for non rubidium-doped perovskites with a decrease with tin introduction from 1.90 eV for $CsPbI_2Br$ to 1.36 eV for $CsSnI_2Br$. Bandgap is once again not affected by rubidium introduction in those compounds where the perovskite structure is not distorted much because of it. On the contrary a prominent increase of the bandgap is observed when introducing Rb in those cases where a distortion of the structure is produced, even more pronounced for those two structures previously catalogued as highly distorted.

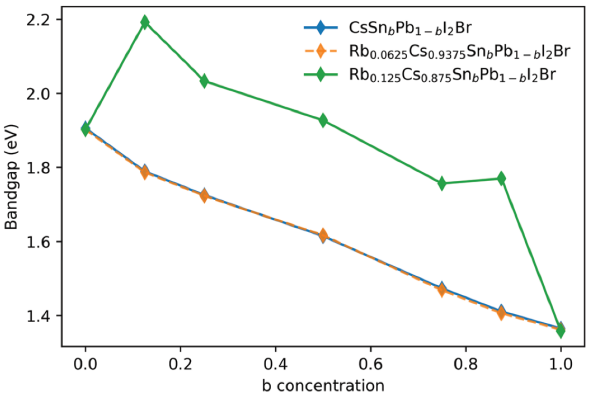

Fig. 9 Bandgaps values for $CsSn_bPb_{1-b}I_2Br$ (red), $Rb_{0.125}Cs_{0.875}Sn_bPb_{1-b}I_2Br$ (blue) and $Rb_{0.0625}Cs_{0.9375}Sn_bPb_{1-b}I_2Br$ (green) compounds calculated using PBE+U (U = 5.6/11 eV for Pb/Sn atoms).

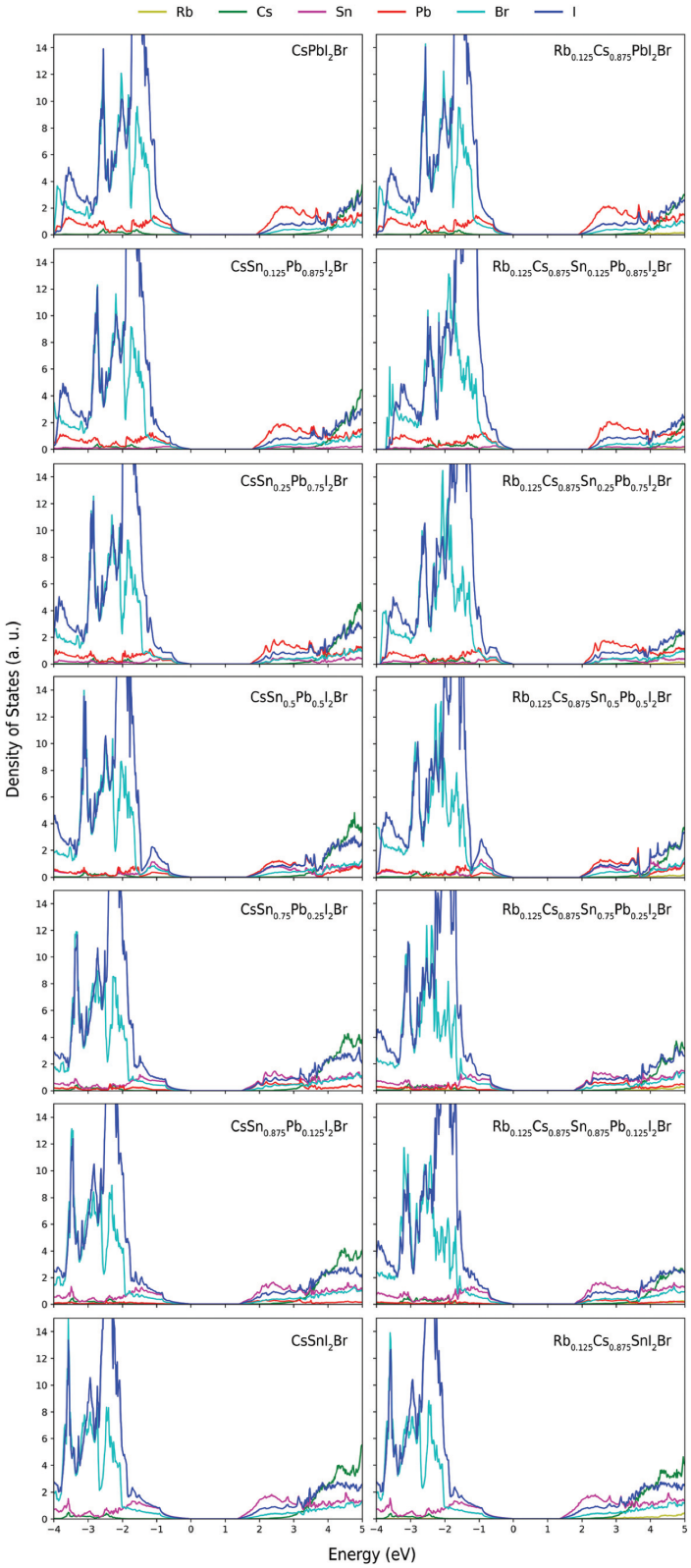

Fig. 10 Density of states for $Rb_aCs_{1-a}Sn_bPb_{1-b}I_2Br$ calculated with PBE+U (U = 5.6/11 eV for Pb/Sn atoms). The zero of energy was set at the Fermi level energy.

To go deeper in this question additional calculations have been performed on bigger 80 atom cells with a monovalent cation Rb/Cs ratio of 0.0625/0.9375. The bandgaps of those compounds have been obtained using exactly the same methodology and U values as for the compounds previously analysed, whether with or without rubidium. The resulting values of the bandgap, with deviations in the bandgap value below the 0.33% in comparison to the corresponding compounds without Rb, confirm that distortion because of Rb, and not introduction of Rb electronic levels, is the main cause of bandgap changes.

Next, the electronic configuration of all the studied compounds will be addressed, to get some chemical knowledge on the effect of the different atom substitutions accomplished. The projected density of states (PDOS) is displayed in Fig. 10. For the sake of simplicity, especially considering that direct bandgaps are shown by all the compounds, electronic band structures are given in the ESI (Fig. S1.1–S1.14†). From PDOS graphs presented in Fig. 10 we can see, as it is already commonly known about perovskites, that CB minima in all the compounds are mainly defined by lead/tin states, while VB maxima are a combination of the same divalent cation and the halide anion orbitals. Specifically, p-type orbitals of Pb/Sn constitute the CB and hybridization of s-type orbitals of Pb/Sn and p-type ones of I/Br constitutes the VB. This way halide valence electrons also play a major role in the bandgap width, defining the position of the VB, although not much the shape of the bands. Monovalent cations, like Cs or Rb here, have on the contrary no direct effect on those border levels, as anticipated by previous analysis. Both CB and VB aren't very dense, a fact that can be seen even clearer in the band structures, with extreme levels being quite uneven in energy along the main k-point directions.

Comparing the different compounds and paying attention to the effect of the different type of cation substitutions, we can see how plots for pure Sn and Pb compounds with and without Rb are practically identical, while when distortion is introduced as previously explained some differences can be noticed. In this line, compounds with Rb present the main peak of states in the VB, generated by the halogen orbitals, a bit closer to the VB maxima than the case of the compounds without it. That difference is around 0.2–0.3 eV for the different ratios of Pb/Sn. This fact could make those compounds present stronger absorption spectra than their analogous compounds without Rb, because of the additional electrons with higher chances of being promoted to the CB. Looking to Pb/Sn substitution, higher densities of states can be observed in the CB minima level corresponding to Pb atoms (p-type orbitals) than to Sn in the compounds with a complementary ratio of Pb/Sn. This detail could suggest that Pb compounds shall present higher absorption rates at energies close to that of the bandgap width than Sn compounds, but that difference is not very pronounced and the arbitrary units of the density of states don't help to elucidate the importance of the fact. This way, no significant difference beside the displacement of the bands resulting in the bandgap width change should be remarked.

Going beyond the electronic configuration of these compounds, one of the main parameters targeted in solar cell devices is absorption. The absorption coefficient of all these compounds has been obtained by means of their dielectric constant, according to the Kramers–Kronig relationship.[109]

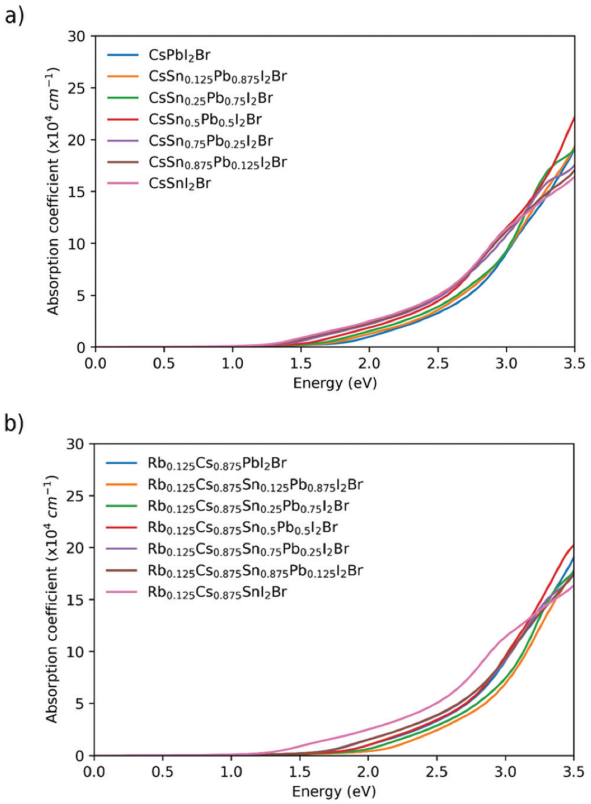

Fig. 11 Absorption coefficients of a) $CsSn_bPb_{1-b}I_2Br$ and b) $Rb_aCs_{1-a}Sn_bPb_{1-b}I_2Br$ (a = 0.125) perovskites.

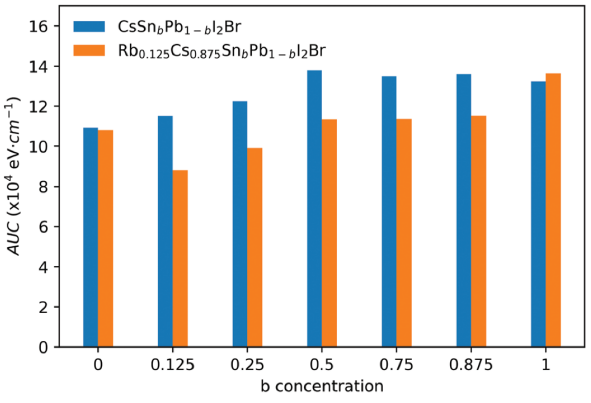

Fig. 12 Area under the curve (AUC) for the absorption coefficients.

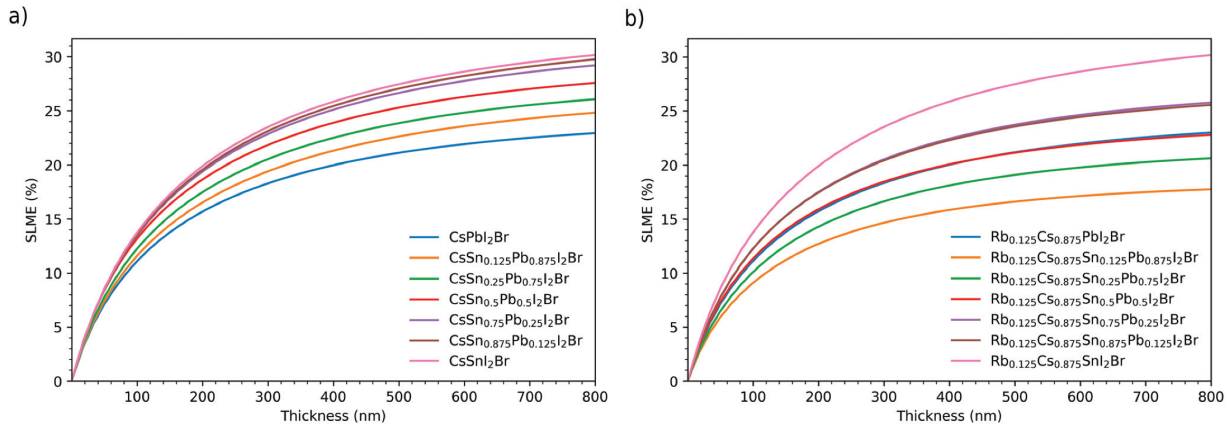

Fig. 13 Spectroscopic limited maximum efficiency (SLME) of a) $CsSn_bPb_{1-b}I_2Br$ and b) $Rb_aCs_{1-a}Sn_bPb_{1-b}I_2Br$ (a = 0.125) perovskites at different values of thickness

Spectra for the whole series of b concentration without rubidium are presented in Fig. 11a, while those of their analogous compounds with 0.125 concentration of rubidium are displayed in Fig. 11b.

From these figures, the influence of distortion can be seen too. Very linear shifting in bandgap energy can be seen here from higher lead concentration compounds to higher tin compounds for the case without Rb, agreeing with the results from the previous section. Compounds with Rb don't follow that linear trend because of the distortion, with b = 0.125 being the one with the lowest absorption because of its higher gap. It is also seen that tin compounds present a higher absorption, meaning a greater increase of the slope in the graph, for higher energies than lead compounds in both cases with and without Rb. From Fig. 11 it is observed that compounds with and without rubidium where no distortion occurs present identical spectra, which could be intuited from PDOS graphs but clearly seen now. To quantify the absorption for every compound AUC for each of them is presented in Fig. 12, where we can see lower AUC values for distorted Rb compounds because of the higher bandgap values. $Rb_aCs_{1-a}PbI_2Br$ (a = 0, 0.125) yields AUC $\simeq 11 \times 10^4$ eV cm^{-1}. It also represents clearly the improvement in the absorption properties of the compounds as the Sn concentration grows, compared to Pb compounds. A difference of almost 2×10^4 eV cm^{-1} can be noticed between the pure tin compounds and the pure lead ones in that sense. In coherence with the effects of Cs replacement by Rb on the bandgap, except for pure Pb and Sn perovskites, AUC decreases to $\simeq 2 \times 10^4$ eV cm^{-1} upon Rb doping.

Based on the calculated bandgaps and absorption coefficients, the spectroscopic limited maximum efficiency (SLME) of the studied compounds has been calculated, according to Yu and Zunger's method.[110] SLME has been obtained for a fixed ambient temperature (293 K) and at different values of thickness of the absorber layer ranging from few nanometers to almost a micrometer. The results are presented in Fig. 13, where it can be seen that maximum values of SLME change mostly with the bandgap of the compound, owning those with lowest bandgaps the highest SLME. That way pure tin compounds present a maximum SLME of 30.17%, while a minimum value of 17.76% is for $Rb_{0.125}Cs_{0.875}Sn_{0.125}Pb_{0.875}I_2Br$. Very similar band structures for all the compounds lead to differences in the absorption spectra besides the absorption edge defined by the bandgap that are not big enough to have an important impact on the SLME.

As said, the Pb dominated direct bandgap transition is the key for an improved light absorption and therefore improved PCE values. Thus, $Rb_aCs_{1-a}Sn_bPb_{1-b}I_2Br$ (a = 0.125, $0.5 \leq b < 1$) would be an adequate chemical composition to obtain AUC and SLME values higher than those obtained for $CsPbI_2Br$, *i.e.*, improved sun-light absorption with a reduced Pb concentration (which would allow a Pb-dominated transition) as well as an improved intrinsic stability due to Rb presence.

Conclusions

Suitability of all-inorganic perovskites with the general formula $Rb_aCs_{1-a}Sn_bPb_{1-b}I_2Br$ (a = 0–0.125 and b = 0–1) to be used as photovoltaic materials with improved intrinsic stability and sun light-absorption properties has been studied here by accurate *ab initio* methods. This way, a detailed picture of the variation of key properties related to structural distortion, thermodynamic formation enthalpies, electronic structure, and sun-light absorption as a function of the chemical composition is provided. We hope that all this information could guide experimental laboratories in the search of new all-inorganic perovskites with the desired properties, as well as with a reduced Pb-concentration. The main conclusions extracted from the results presented above are emphasized as follows:

- For mixed Sn–Pb perovskites, introduction of Rb leads to a distortion in the structure due to the smaller size of the Rb cation compared to the Cs one, which doesn't occur in the

pure Sn and Pb perovskites. Higher rates of structural distortion lead to more negative formation enthalpies, meaning higher intrinsic stability. This could be an interesting effect looking at the well-known problems of stability of perovskites, if controlled and fine-tuned propitiously upon chemical composition.

• To study cation substitution effects on the electronic structure and absorption features, several *ab initio* methods (PBE, PBE+*U*, HSE06, *GW*, and spin–orbit coupling effects) have been assessed bearing in mind a good compromise between accuracy and computational efforts. Thus, we prove that PBE+*U* is a very cost-effective method to describe correctly the optical properties of these perovskites, especially Sn based compounds.

• For $CsSn_bPb_{1-b}I_2Br$ perovskites, replacement of Pb by Sn leads to lower bandgap values. Lower bandgaps of Sn based perovskites are responsible for their improved sun-light absorption features, as we saw with AUC up to 2×10^4 eV cm^{-1} higher than that of pure Pb perovskite. For pure Pb and Sn perovskites (*i.e.*, $CsPbI_2Br$ and $CsSnI_2Br$), introduction of Rb in the perovskite structure has no direct effect on the band gap of the compound. Nonetheless, Rb concentration rates higher than 6.25% (among monovalent cations) lead to a significant increase of the material band gap.

In summary, this paper reports an intensive analysis aiming to quantify distortions in all-inorganic perovskites with chemical composition, linked to changes in stability- and absorption-related properties. Thus, our results evidence that all-inorganic $Rb_{0.125}Cs_{0.875}Sn_bPb_{1-b}I_2Br$ ($0.5 < b < 1$) perovskites with Rb doping and reduced Pb concentration would be excellent candidates to be used in high-efficiency photovoltaic devices, as active materials with improved stability, reduced toxicity and enhanced sun-light absorption features.

Conflicts of interest

There are no conflicts to declare.

Acknowledgements

This work was supported by the Ministerio de Ciencia e Innovación through the project BESTMAT-QC (PID2019-107137RB-C22). The authors gratefully acknowledge the Universidad Politécnica de Madrid (http://www.upm.es) for providing computing resources on Magerit Supercomputer. The authors thankfully acknowledge the computer resources at Lusitania II (CénitS) and the technical support provided by Lusitania II (CénitS) (RES-FI-2021-2-0009). The statements made herein are solely the responsibility of the authors.

References

1 A. Kojima, K. Teshima, Y. Shirai and T. Miyasaka, Organometal Halide Perovskites as Visible-Light Sensitizers for Photovoltaic Cells, *J. Am. Chem. Soc.*, 2009, **131**, 6050–6051.

2 J. H. Heo, S. H. Im, J. H. Noh, T. N. Mandal, C. S. Lim, J. A. Chang, Y. H. Lee, H. J. Kim, A. Sarkar, M. K. Nazeeruddin, M. Grätzel and S. Il Seok, Efficient inorganic-organic hybrid heterojunction solar cells containing perovskite compound and polymeric hole conductors, *Nat. Photonics*, 2013, **7**, 486–491.

3 J. P. Correa-Baena, A. Abate, M. Saliba, W. Tress, T. Jesper Jacobsson, M. Grätzel and A. Hagfeldt, The rapid evolution of highly efficient perovskite solar cells, *Energy Environ. Sci.*, 2017, **10**, 710–727.

4 NREL, Best Research-Cell Efficiency Chart, https://www.nrel.gov/pv/assets/pdfs/best-research-cell-efficiencies.20200311.pdf, (accessed 30 April 2021).

5 E. Bellini, UNIST, EPFL claim 25.6% efficiency world record for perovskite solar cell, https://www.pv-magazine.com/2021/04/06/unist-epfl-claim-25-6-efficiency-world-record-for-perovskite-solar-cell/.

6 M. Hutchins, Oxford PV retakes tandem cell efficiency record, https://www.pv-magazine.com/2020/12/21/oxford-pv-retakes-tandem-cell-efficiency-record/.

7 T. Wang, B. Daiber, J. M. Frost, S. A. Mann, E. C. Garnett, A. Walsh and B. Ehrler, Indirect to direct bandgap transition in methylammonium lead halide perovskite, *Energy Environ. Sci.*, 2017, **10**, 509–515.

8 E. Menéndez-Proupin, P. Palacios, P. Wahnón and J. C. Conesa, Self-consistent relativistic band structure of the CH3NH3PbI3 perovskite, *Phys. Rev. B: Condens. Matter Mater. Phys.*, 2014, **90**, 045207.

9 A. Jiménez-Solano, S. Carretero-Palacios and H. Míguez, Absorption enhancement in methylammonium lead iodide perovskite solar cells with embedded arrays of dielectric particles, *Opt. Express*, 2018, **26**, A865–A878.

10 M. D. Nelson and M. Di Vece, Using a Neural Network to Improve the Optical Absorption in Halide Perovskite Layers Containing Core-Shells Silver Nanoparticles, *Nanomaterials*, 2019, **9**, 437.

11 A. Filippetti, A. Mattoni, C. Caddeo, M. I. Saba and P. Delugas, Low electron-polar optical phonon scattering as a fundamental aspect of carrier mobility in methylammonium lead halide CH3NH3PbI3 perovskites, *Phys. Chem. Chem. Phys.*, 2016, **18**, 15352–15362.

12 G. Xing, N. Mathews, S. Sun, S. S. Lim, Y. M. Lam, M. Graẗzel, S. Mhaisalkar and T. C. Sum, Long-range balanced electron- and hole-transport lengths in organic-inorganic $CH_3NH_3PbI_3$, *Science*, 2013, **342**, 344–347.

13 A. L. Montero-Alejo, E. Menéndez-Proupin, P. Palacios, P. Wahnón and J. C. Conesa, Ferroelectric Domains May Lead to Two-Dimensional Confinement of Holes, but not of Electrons, in CH3NH3PbI3 Perovskite, *J. Phys. Chem. C*, 2017, **121**, 26698–26705.

14 O. V. P. Yutong Wang, W.-H. Fang and R. Long, Symmetry Breaking at $MAPbI_3$ Perovskite Grain Boundaries Suppresses Charge Recombination: Time-Domain ab Initio Analysis, *J. Phys. Chem. Lett.*, 2019, **10**, 1617–1623.

15 M. B. Johnston and L. M. Herz, Hybrid Perovskites for Photovoltaics: Charge-Carrier Recombination, Diffusion, and Radiative Efficiencies, *Acc. Chem. Res.*, 2016, **49**, 146–154.
16 E. Menéndez-Proupin, C. L. B. Ríos and P. Wahnón, Nonhydrogenic exciton spectrum in perovskite CH3NH3PbI3, *Phys. Status Solidi RRL*, 2015, **9**, 559–563.
17 X. Zhao and N. G. Park, Stability issues on perovskite solar cells, *Photonics*, 2015, **2**, 1139–1151.
18 A. Babayigit, A. Ethirajan, M. Muller and B. Conings, Toxicity of organometal halide perovskite solar cells, *Nat. Mater.*, 2016, **15**, 247–251.
19 P. Roy, N. Kumar Sinha, S. Tiwari and A. Khare, A review on perovskite solar cells: Evolution of architecture, fabrication techniques, commercialization issues and status, *Sol. Energy*, 2020, **198**, 665–688.
20 M. G. Ju, M. Chen, Y. Zhou, J. Dai, L. Ma, N. P. Padture and X. C. Zeng, Toward Eco-friendly and Stable Perovskite Materials for Photovoltaics, *Joule*, 2018, **2**, 1231–1241.
21 Y. Zhou and Y. Zhao, Chemical stability and instability of inorganic halide perovskites, *Energy Environ. Sci.*, 2019, **12**, 1495–1511.
22 Q. Wali, F. J. Iftikhar, M. E. Khan, A. Ullah, Y. Iqbal and R. Jose, Advances in stability of perovskite solar cells, *Org. Electron.*, 2020, **78**, 105590.
23 Q. Fu, X. Tang, B. Huang, T. Hu, L. Tan, L. Chen and Y. Chen, Recent Progress on the Long-Term Stability of Perovskite Solar Cells, *Adv. Sci.*, 2018, **5**, 1700387.
24 A. Urbina, The balance between efficiency, stability and environmental impacts in perovskite solar cells: a review, *J. Phys.: Energy*, 2020, **2**, 022001.
25 B. Brunetti, C. Cavallo, A. Ciccioli, G. Gigli and A. Latini, On the Thermal and Thermodynamic (In)Stability of Methylammonium Lead Halide Perovskites, *Sci. Rep.*, 2016, **6**, 31896.
26 A. Mattoni, A. Filippetti, M. I. Saba and P. Delugas, Methylammonium Rotational Dynamics in Lead Halide Perovskite by Classical Molecular Dynamics: The Role of Temperature, *J. Phys. Chem. C*, 2015, **119**, 17421–17428.
27 M. A. Carignano, A. Kachmar and J. Hutter, Thermal effects on $CH_3NH_3PbI_3$ perovskite from Ab initio molecular dynamics simulations, *J. Phys. Chem. C*, 2015, **119**, 8991–8997.
28 M. Mladenović and N. Vukmirović, Effects of thermal disorder on the electronic structure of halide perovskites: Insights from MD simulations, *Phys. Chem. Chem. Phys.*, 2018, **20**, 25693–25700.
29 A. L. Montero-Alejo, E. Menéndez-Proupin, D. Hidalgo-Rojas, P. Palacios, P. Wahnón and J. C. Conesa, Modeling of Thermal Effect on the Electronic Properties of Photovoltaic Perovskite CH3NH3PbI3: The Case of Tetragonal Phase, *J. Phys. Chem. C*, 2016, **120**, 7976–7986.
30 T. Leijtens, G. E. Eperon, N. K. Noel, S. N. Habisreutinger, A. Petrozza and H. J. Snaith, Stability of metal halide perovskite solar cells, *Adv. Energy Mater.*, 2015, **5**, 1–23.
31 J. Liang, C. Wang, Y. Wang, Z. Xu, Z. Lu, Y. Ma, H. Zhu, Y. Hu, C. Xiao, X. Yi, G. Zhu, H. Lv, L. Ma, T. Chen, Z. Tie, Z. Jin and J. Liu, All-Inorganic Perovskite Solar Cells, *J. Am. Chem. Soc.*, 2016, **138**, 15829–15832.
32 S. Gupta, T. Bendikov, G. Hodes and D. Cahen, $CsSnBr_3$, A Lead-Free Halide Perovskite for Long-Term Solar Cell Application: Insights on SnF_2 Addition, *ACS Energy Lett.*, 2016, **1**, 1028–1033.
33 J. Liang, P. Zhao, C. Wang, Y. Wang, Y. Hu, G. Zhu, L. Ma, J. Liu and Z. Jin, $CsPb_{0.9}Sn_{0.1}IBr_2$ Based All-Inorganic Perovskite Solar Cells with Exceptional Efficiency and Stability, *J. Am. Chem. Soc.*, 2017, **139**, 14009–14012.
34 J. Tian, J. Wang, Q. Xue, T. Niu, L. Yan, Z. Zhu, N. Li, C. J. Brabec, H. L. Yip and Y. Cao, Composition Engineering of All-Inorganic Perovskite Film for Efficient and Operationally Stable Solar Cells, *Adv. Funct. Mater.*, 2020, **30**, 2001764.
35 J. Duan, H. Xu, W. E. I. Sha, Y. Zhao, Y. Wang, X. Yang and Q. Tang, Inorganic perovskite solar cells: An emerging member of the photovoltaic community, *J. Mater. Chem. A*, 2019, **7**, 21036–21068.
36 G. Niu, W. Li, J. Li, X. Liang and L. Wang, Enhancement of thermal stability for perovskite solar cells through cesium doping, *RSC Adv.*, 2017, **7**, 17473–17479.
37 T. T. Ava, A. Al Mamun, S. Marsillac and G. Namkoong, A Review: Thermal Stability of Methylammonium Lead Halide Based Perovskite Solar Cells, *Appl. Sci.*, 2019, **9**, 188.
38 T. Ma, S. Wang, Y. Zhang, K. Zhang and L. Yi, The development of all-inorganic $CsPbX_3$ perovskite solar cells, *J. Mater. Sci.*, 2020, **55**, 464–479.
39 K. Wang, Z. Jin, L. Liang, H. Bian, D. Bai, H. Wang, J. Zhang, Q. Wang and L. Shengzhong, All-inorganic cesium lead iodide perovskite solar cells with stabilized efficiency beyond 15%, *Nat. Commun.*, 2018, **9**, 1–8.
40 Y. Wang, X. Liu, T. Zhang, X. Wang, M. Kan, J. Shi and Y. Zhao, The Role of Dimethylammonium Iodide in $CsPbI^3$ Perovskite Fabrication: Additive or Dopant?, *Angew. Chem., Int. Ed.*, 2019, **58**, 16691–16696.
41 S. Fu, L. Wan, W. Zhang, X. Li, W. Song and J. Fang, Tailoring in Situ Healing and Stabilizing Post-Treatment Agent for High-Performance Inverted $CsPbI_3$ Perovskite Solar Cells with Efficiency of 16.67%, *ACS Energy Lett.*, 2020, **5**, 3314–3321.
42 X. Chang, J. Fang, Y. Fan, T. Luo, H. Su, Y. Zhang, J. Lu, L. Tsetseris, T. D. Anthopoulos, S. Liu and K. Zhao, Printable $CsPbI_3$ Perovskite Solar Cells with PCE of 19% via an Additive Strategy, *Adv. Mater.*, 2020, **32**, 1–8.
43 L. Chen, L. Wan, X. Li, W. Zhang, S. Fu, Y. Wang, S. Li, H. Q. Wang, W. Song and J. Fang, Inverted All-Inorganic $CsPbI_2Br$ Perovskite Solar Cells with Promoted Efficiency and Stability by Nickel Incorporation, *Chem. Mater.*, 2019, 2–9.
44 Z. Zeng, J. Zhang, X. Gan, H. Sun, M. Shang, D. Hou, C. Lu, R. Chen, Y. Zhu and L. Han, In Situ Grain Boundary Functionalization for Stable and Efficient Inorganic $CsPbI_2Br$ Perovskite Solar Cells, *Adv. Energy Mater.*, 2018, **8**, 1–8.

45 R. J. Sutton, G. E. Eperon, L. Miranda, E. S. Parrott, B. A. Kamino, J. B. Patel, M. T. Hörantner, M. B. Johnston, A. A. Haghighirad, D. T. Moore and H. J. Snaith, Bandgap-Tunable Cesium Lead Halide Perovskites with High Thermal Stability for Efficient Solar Cells, *Adv. Energy Mater.*, 2016, **6**, 1–6.

46 E. Mosconi, A. Amat, M. K. Nazeeruddin, M. Grätzel and F. De Angelis, First-principles modeling of mixed halide organometal perovskites for photovoltaic applications, *J. Phys. Chem. C*, 2013, **117**, 13902–13913.

47 W. J. Yin, Y. Yan and S. H. Wei, Anomalous alloy properties in mixed halide perovskites, *J. Phys. Chem. Lett.*, 2014, **5**, 3625–3631.

48 S. Mariotti, O. S. Hutter, L. J. Phillips, P. J. Yates, B. Kundu and K. Durose, Stability and Performance of CsPbI2Br Thin Films and Solar Cell Devices, *ACS Appl. Mater. Interfaces*, 2018, **10**, 3750–3760.

49 Y. Wang, T. Zhang, F. Xu, Y. Li and Y. Zhao, A Facile Low Temperature Fabrication of High Performance $CsPbI_2Br$ All-Inorganic Perovskite Solar Cells, *Sol. RRL*, 2018, **2**, 1–6.

50 J. He, J. Liu, Y. Hou, Y. Wang, S. Yang and H. G. Yang, Surface chelation of cesium halide perovskite by dithiocarbamate for efficient and stable solar cells, *Nat. Commun.*, 2020, **11**, 1–8.

51 W. Chen, H. Chen, G. Xu, R. Xue, S. Wang, Y. Li and Y. Li, Precise Control of Crystal Growth for Highly Efficient CsPbI 2 Br Perovskite Solar Cells, *Joule*, 2019, **3**, 191–204.

52 G. Yin, H. Zhao, H. Jiang, S. Yuan, T. Niu, K. Zhao, Z. Liu and S. Liu, Precursor Engineering for All-Inorganic $CsPbI_2Br$ Perovskite Solar Cells with 14.78% Efficiency, *Adv. Funct. Mater.*, 2018, **28**, 1–10.

53 C. Liu, W. Li, C. Zhang, Y. Ma, J. Fan and Y. Mai, All-Inorganic $CsPbI_2Br$ Perovskite Solar Cells with High Efficiency Exceeding 13%, *J. Am. Chem. Soc.*, 2018, **140**, 3825–3828.

54 J. Zhang, D. Bai, Z. Jin, H. Bian, K. Wang, J. Sun, Q. Wang and S. F. Liu, 3D–2D–0D Interface Profiling for Record Efficiency All-Inorganic $CsPbBrI_2$ Perovskite Solar Cells with Superior Stability, *Adv. Energy Mater.*, 2018, **8**, 1–9.

55 T. D. Siegler, D. W. Houck, S. H. Cho, D. J. Milliron and B. A. Korgel, Bismuth Enhances the Stability of $CH_3NH_3PbI_3$ (MAPI) Perovskite under High Humidity, *J. Phys. Chem. C*, 2019, **123**, 963–970.

56 Z. Guo, S. Zhao, A. Liu, Y. Kamata, S. Teo, S. Yang, Z. Xu, S. Hayase and T. Ma, Niobium Incorporation into $CsPbI_2Br$ for Stable and Efficient All-Inorganic Perovskite Solar Cells, *ACS Appl. Mater. Interfaces*, 2019, **11**, 19994–20003.

57 Y. Guo, H. Liu, W. Li, L. Zhu and H. Chen, Additive Engineering Toward High-Performance $CsPbI_3$ Perovskite Solar Cells, *Sol. RRL*, 2020, **4**, 2000380.

58 S. S. Mali, J. V. Patil and C. K. Hong, Hot-Air-Assisted Fully Air-Processed Barium Incorporated $CsPbI_2Br$ Perovskite Thin Films for Highly Efficient and Stable All-Inorganic Perovskite Solar Cells, *Nano Lett.*, 2019, **19**, 6213–6220.

59 J. K. Nam, S. U. Chai, W. Cha, Y. J. Choi, W. Kim, M. S. Jung, J. Kwon, D. Kim and J. H. Park, Potassium Incorporation for Enhanced Performance and Stability of Fully Inorganic Cesium Lead Halide Perovskite Solar Cells, *Nano Lett.*, 2017, **17**, 2028–2033.

60 Y. Hu, F. Bai, X. Liu, Q. Ji, X. Miao, T. Qiu and S. Zhang, Bismuth Incorporation Stabilized α-$CsPbI_3$ for Fully Inorganic Perovskite Solar Cells, *ACS Energy Lett.*, 2017, **2**, 2219–2227.

61 P. N. Rudd and J. Huang, Metal Ions in Halide Perovskite Materials and Devices, *Trends Chem.*, 2019, **1**, 394–409.

62 Z. Zeng, Y. Xu, Z. Zhang, Z. Gao, M. Luo, Z. Yin, C. Zhang, J. Xu, B. Huang, F. Luo, Y. Du and C. Yan, Rare-earth-containing perovskite nanomaterials: Design, synthesis, properties and applications, *Chem. Soc. Rev.*, 2020, **49**, 1109–1143.

63 X. Chen, J. Xu, Y. Xu, F. Luo and Y. Du, Rare earth double perovskites: A fertile soil in the field of perovskite oxides, *Inorg. Chem. Front.*, 2019, **6**, 2226–2238.

64 M. Saliba, T. Matsui, K. Domanski, J. Y. Seo, A. Ummadisingu, S. M. Zakeeruddin, J. P. Correa-Baena, W. R. Tress, A. Abate, A. Hagfeldt and M. Grätzel, Incorporation of rubidium cations into perovskite solar cells improves photovoltaic performance, *Science*, 2016, **354**, 206–209.

65 J. V. Patil, S. S. Mali and C. K. Hong, A-Site Rubidium Cation-Incorporated $CsPbI_2Br$ All-Inorganic Perovskite Solar Cells Exceeding 17% Efficiency, *Sol. RRL*, 2020, **4**, 2000164.

66 D. B. Khadka, Y. Shirai, M. Yanagida and K. Miyano, Attenuating the defect activities with a rubidium additive for efficient and stable Sn-based halide perovskite solar cells, *J. Mater. Chem. C*, 2020, **8**, 2307–2313.

67 W. Zhang, J. Xiong, J. Li and W. A. Daoud, Guanidinium Passivation for Air-Stable Rubidium-Incorporated $Cs_{(1-x)}Rb_xPbI_2Br$ Inorganic Perovskite Solar Cells, *Sol. RRL*, 2020, **4**, 2000112.

68 P. Sánchez-Palencia, G. García, P. Wahnón and P. Palacios, The effects of the chemical composition on the structural, thermodynamic, and mechanical properties of all-inorganic halide perovskites, *Inorg. Chem. Front.*, 2021, **8**, 3803–3814.

69 W. Ke and M. G. Kanatzidis, Prospects for low-toxicity lead-free perovskite solar cells, *Nat. Commun.*, 2019, **10**, 1–4.

70 M. Roknuzzaman, K. K. Ostrikov, H. Wang, A. Du and T. Tesfamichael, Towards lead-free perovskite photovoltaics and optoelectronics by ab-initio simulations, *Sci. Rep.*, 2017, **7**, 1–8.

71 S. A. A. Shah, M. H. Sayyad, K. Khan, K. Guo, F. Shen, J. Sun, A. K. Tareen, Y. Gong and Z. Guo, Progress towards high-efficiency and stable tin-based perovskite solar cells, *Energies*, 2020, **13**, 5092.

72 D. Sabba, H. K. Mulmudi, R. R. Prabhakar, T. Krishnamoorthy, T. Baikie, P. P. Boix, S. Mhaisalkar and N. Mathews, Impact of anionic Br- substitution on open circuit voltage in lead free perovskite ($CsSnI_{3-x}Br_x$) solar cells, *J. Phys. Chem. C*, 2015, **119**, 1763–1767.

73 F. Giustino and H. J. Snaith, Toward Lead-Free Perovskite Solar Cells, *ACS Energy Lett.*, 2016, **1**, 1233–1240.

74 C. Gai, J. Wang, Y. Wang and J. Li, The low-dimensional three-dimensional tin halide perovskite: Film characterization and device performance, *Energies*, 2020, **13**, 2.

75 L. Serrano-Lujan, N. Espinosa, T. T. Larsen-Olsen, J. Abad, A. Urbina and F. C. Krebs, Tin- and lead-based perovskite solar cells under scrutiny: An environmental perspective, *Adv. Energy Mater.*, 2015, **5**, 1–5.

76 A. Filippetti and A. Mattoni, Hybrid perovskites for photovoltaics: Insights from first principles, *Phys. Rev. B: Condens. Matter Mater. Phys.*, 2014, **89**, 1–8.

77 W. Hu, X. He, Z. Fang, W. Lian, Y. Shang, X. Li, W. Zhou, M. Zhang, T. Chen, Y. Lu, L. Zhang, L. Ding and S. Yang, Bulk heterojunction gifts bismuth-based lead-free perovskite solar cells with record efficiency, *Nano Energy*, 2020, **68**, 104362.

78 X. Yang, W. Wang, R. Ran, W. Zhou and Z. Shao, Recent Advances in $Cs_2AgBiBr_6$-Based Halide Double Perovskites as Lead-Free and Inorganic Light Absorbers for Perovskite Solar Cells, *Energy Fuels*, 2020, **34**, 10513–10528.

79 F. De Angelis, The Prospect of Lead-Free Perovskite Photovoltaics, *ACS Energy Lett.*, 2021, 1586–1587.

80 B. Parida, S. Yoon, S. M. Jeong, J. S. Cho, J. K. Kim and D. W. Kang, Recent progress on cesium lead/tin halide-based inorganic perovskites for stable and efficient solar cells: A review, *Sol. Energy Mater. Sol. Cells*, 2020, **204**, 110212.

81 M. Konstantakou and T. Stergiopoulos, A critical review on tin halide perovskite solar cells, *J. Mater. Chem. A*, 2017, **5**, 11518–11549.

82 X. Jiang, H. Li, Q. Zhou, Q. Wei, M. Wei, L. Jiang, Z. Wang, Z. Peng, F. Wang, Z. Zang, K. Xu, Y. Hou, S. Teale, W. Zhou, R. Si, X. Gao, E. H. Sargent and Z. Ning, One-Step Synthesis of SnI_2·(DMSO)xAdducts for High-Performance Tin Perovskite Solar Cells, *J. Am. Chem. Soc.*, 2021, **143**, 10970–10976.

83 T. Ye, X. Wang, K. Wang, S. Ma, D. Yang, Y. Hou, J. Yoon, K. Wang and S. Priya, Localized Electron Density Engineering for Stabilized B-γ$CsSnI_3$-Based Perovskite Solar Cells with Efficiencies >10%, *ACS Energy Lett.*, 2021, **6**, 1480–1489.

84 K. Xiao, R. Lin, Q. Han, Y. Hou, Z. Qin, H. T. Nguyen, J. Wen, M. Wei, V. Yeddu, M. I. Saidaminov, Y. Gao, X. Luo, Y. Wang, H. Gao, C. Zhang, J. Xu, J. Zhu, E. H. Sargent and H. Tan, All-perovskite tandem solar cells with 24.2% certified efficiency and area over 1 cm2 using surface-anchoring zwitterionic antioxidant, *Nat. Energy*, 2020, **5**, 870–880.

85 R. M. I. Bandara, S. M. Silva, C. C. L. Underwood, K. D. G. I. Jayawardena, R. A. Sporea and S. R. P. Silva, Progress of Pb-Sn Mixed Perovskites for Photovoltaics: A Review, *Energy Environ. Mater.*, 2021, **0**, 1–31.

86 P. Hohenberg and W. Kohn, Inhomogeneous Electron Gas, *Phys. Rev.*, 1964, **136**, 864–871.

87 W. Kohn and L. J. Sham, Self-Consistent Equations Including Exchange and Correlation Effects, *Phys. Rev.*, 1965, **140**, 1133–1138.

88 J. P. Perdew, A. Ruzsinszky, G. I. Csonka, O. A. Vydrov, G. E. Scuseria, L. A. Constantin, X. Zhou and K. Burke, Restoring the density-gradient expansion for exchange in solids and surfaces, *Phys. Rev. Lett.*, 2008, **100**, 1–4.

89 J. P. Perdew, K. Burke and M. Ernzerhof, Generalized gradient approximation made simple, *Phys. Rev. Lett.*, 1996, **77**, 3865–3868.

90 H. J. Monkhorst and J. D. Pack, Special points for Brillouin-zone integrations, *Phys. Rev. B: Solid State*, 1976, **13**, 5188–5192.

91 S. Dudarev and G. Botton, Electron-energy-loss spectra and the structural stability of nickel oxide: An LSDA+U study, *Phys. Rev. B: Condens. Matter Mater. Phys.*, 1998, **57**, 1505–1509.

92 J. Hubbard, Electron correlations in narrow energy bands, *Proc. R. Soc. London, Ser. A*, 1963, **276**, 238–257.

93 L. Hedin, New Method for Calculating the One-Particle Green's Function with Application to the Electron-Gas Problem, *Phys. Rev.*, 1965, **139**, 796–823.

94 J. Heyd, G. E. Scuseria and M. Ernzerhof, Hybrid functionals based on a screened Coulomb potential, *J. Chem. Phys.*, 2003, **118**, 8207–8215.

95 G. García, P. Palacios, E. Menéndez-Proupin, A. L. Montero-Alejo, J. C. Conesa and P. Wahnón, Influence of chromium hyperdoping on the electronic structure of $CH_3NH_3PbI_3$ perovskite: A first-principles insight, *Sci. Rep.*, 2018, **8**, 1–12.

96 J. Wiktor, U. Rothlisberger and A. Pasquarello, Predictive Determination of Band Gaps of Inorganic Halide Perovskites, *J. Phys. Chem. Lett.*, 2017, **8**, 5507–5512.

97 P. Boross, B. Dóra, A. Kiss and F. Simon, A unified theory of spin-relaxation due to spin-orbit coupling in metals and semiconductors, *Sci. Rep.*, 2013, **3**, 1–5.

98 P. E. Blöchl, Projector augmented-wave method, *Phys. Rev. B: Condens. Matter Mater. Phys.*, 1994, **50**, 17953–17979.

99 G. Kresse and J. Furthmüller, Efficiency of *ab initio* total energy calculations for metals and semiconductors using a plane-wave basis set, *Comput. Mater. Sci.*, 1996, **6**, 15–50.

100 G. Kresse and J. Furthmüller, Efficient iterative schemes for ab initio total-energy calculations using a plane-wave basis set, *Phys. Rev. B: Condens. Matter Mater. Phys.*, 1996, **54**, 169–186.

101 J. A. Steele, M. Lai, Y. Zhang, Z. Lin, J. Hofkens, M. B. J. Roeffaers and P. Yang, Phase Transitions and Anion Exchange in All-Inorganic Halide Perovskites, *Acc. Mater. Res.*, 2020, **1**, 3–15.

102 G. E. Eperon, G. M. Paternò, R. J. Sutton, A. Zampetti, A. A. Haghighirad, F. Cacialli and H. J. Snaith, Inorganic caesium lead iodide perovskite solar cells, *J. Mater. Chem. A*, 2015, **3**, 19688–19695.

103 R. Grau-Crespo, S. Hamad, C. R. A. Catlow and N. H. De Leeuw, Symmetry-adapted configurational modelling of

fractional site occupancy in solids, *J. Phys.: Condens. Matter*, 2007, **19**, 256201.
104 V. M. Goldschmidt, Die Gesetze der Krystallochemie, *Naturwissenschaften*, 1926, **14**, 477–485.
105 W. Travis, E. N. K. Glover, H. Bronstein, D. O. Scanlon and R. G. Palgrave, On the application of the tolerance factor to inorganic and hybrid halide perovskites: A revised system, *Chem. Sci.*, 2016, **7**, 4548–4556.
106 J. Even, L. Pedesseau, J. M. Jancu and C. Katan, Importance of spin-orbit coupling in hybrid organic/inorganic perovskites for photovoltaic applications, *J. Phys. Chem. Lett.*, 2013, **4**, 2999–3005.
107 P. Azarhoosh, S. McKechnie, J. M. Frost, A. Walsh and M. Van Schilfgaarde, Research Update: Relativistic origin of slow electron-hole recombination in hybrid halide perovskite solar cells, *APL Mater.*, 2016, **4**, 091501.
108 G. Volonakis, M. R. Filip, A. A. Haghighirad, N. Sakai, B. Wenger, H. J. Snaith and F. Giustino, Lead-Free Halide Double Perovskites via Heterovalent Substitution of Noble Metals, *J. Phys. Chem. Lett.*, 2016, **7**, 1254–1259.
109 M. Gajdoš, K. Hummer, G. Kresse, J. Furthmüller and F. Bechstedt, Linear optical properties in the projector-augmented wave methodology, *Phys. Rev. B: Condens. Matter Mater. Phys.*, 2006, **73**, 1–9.
110 L. Yu and A. Zunger, Identification of potential photovoltaic absorbers based on first-principles spectroscopic screening of materials, *Phys. Rev. Lett.*, 2012, **108**, 1–5.
111 A. Swarnkar, A. R. Marshall, E. M. Sanehira, B. D. Chernomordik, D. T. Moore, J. A. Christians, T. Chakrabarti and J. M. Luther, Quantum dot-induced phase stabilization of α-$CsPbI_3$ perovskite for high-efficiency photovoltaics, *Science*, 2016, **354**, 92–95.
112 J. B. Hoffman, A. L. Schleper and P. V. Kamat, Transformation of Sintered $CsPbBr_3$ Nanocrystals to Cubic $CsPbI_3$ and Gradient $CsPbBr_xI_{3-x}$ through Halide Exchange, *J. Am. Chem. Soc.*, 2016, **138**, 8603–8611.
113 I. Chung, J. H. Song, J. Im, J. Androulakis, C. D. Malliakas, H. Li, A. J. Freeman, J. T. Kenney and M. G. Kanatzidis, $CsSnI_3$: Semiconductor or metal? High electrical conductivity and strong near-infrared photoluminescence from a single material. High hole mobility and phase-transitions, *J. Am. Chem. Soc.*, 2012, **134**, 8579–8587.